

SEMESTER THESIS

Numerical Investigation of the Impact of Grazing Flow on the Damping Performance of Acoustic Resonators

Author:

Maximilian Bambauer

Matrikel-No:

3626580

Supervisors:

Kilian Förner, M. Sc.
Prof. Wolfgang Polifke, Ph. D.

January 23, 2017

Erklärung

Hiermit versichere ich, die vorliegende Arbeit selbstständig verfasst zu haben. Ich habe keine anderen Quellen und Hilfsmittel als die angegebenen verwendet.

Ort, Datum

Maximilian Bambauer

Acknowledgement

I would like to offer my special thanks to Kilian Förner for the advice and feedback given during the completion of this thesis.

Abstract

This work investigates the performance characteristics of Helmholtz resonators, using numerical simulations performed with the open source software OpenFOAM. A scaling method is presented, which allows the simplification of resonator geometries with multiple throats per cavity into a single-cavity single-throat configuration, without changing its impedance. In order to determine the resonator impedance, two different approaches are tested and compared. The impedance tube method uses area averaged pressure and velocity data from a reference surface in the channel, while the in situ method utilizes pressure data from sensors placed on the frontplate and backplate of the resonator. The results show a close match especially at low grazing velocities, with the difference between both increasing as the grazing flow velocity is raised. A particular interest is taken in determining the effects of grazing flow on the resonator behavior. The grazing flow causes a recirculation zone to form inside the throat, decreasing the fluctuating mass and therefore increasing the eigenfrequency of the resonator. This shift is confirmed by the simulation and also matched with analytical calculations. Moreover, whistling is observed at low grazing flow velocities for a configuration considered. An effect that is caused by vortices shedding of the resonator throat edge and hitting the opposite throat wall, which causes a pressure spike. If the timescale of this effect matches with the eigenfrequency of the resonator, a continuous fluctuating pressure wave is emitted. Using the definition of the critical Strouhal number, the reasons for the occurrence of the whistling behavior is explained. Overall, the simulations were successful in reproducing experimental data for resonator geometries with and without grazing flow up to Mach 0.4, showing a closer match than has been achieved in similar publications.

Kurzfassung

In dieser Arbeit werden die Leistungskennzahlen von Helmholtz-Resonatoren untersucht. Hierfür werden numerische Simulationen mit dem Open-Source-Paket OpenFOAM durchgeführt. Es wird eine einfache Skalierungsmethode präsentiert mit deren Hilfe sich Resonator-Geometrien, welche mehrere Öffnungen pro Hohlraum besitzen, zu Geometrien mit nur einer Öffnung pro Hohlraum vereinfachen lassen, ohne dabei deren Resonanzverhalten zu verändern. Um die Impedanz des Resonators zu ermitteln, werden zwei unterschiedliche Ansätze getestet und verglichen. Zum einen wird die Impedanzrohr-Methode herangezogen, welche flächengemittelt Druck und Geschwindigkeit, gemessen auf einer Referenzebene, zur Bestimmung der Impedanz nutzt. Zum Anderen die in situ Methode, welche mit Druckmessungen an der Stirnfläche und dem Boden des Hohlraumes arbeitet. Die somit ermittelten Impedanzwerte zeigen eine gute Übereinstimmung untereinander, wobei eine steigende Abweichung bei Erhöhung der Überströmungsgeschwindigkeit festgestellt werden kann. Ein besonderes Augenmerk liegt in der Ermittlung von Überströmungseffekten auf das Resonatorverhalten. Durch die Überströmung wird ein Zirkulationsgebiet im Hals des Resonators erzeugt, welcher die fluktuierende Gesamtmasse verringert, was wiederum zu einer Erhöhung der Eigenfrequenz führt. Dieses Verhalten kann in den Simulationen bestätigt werden, welche wiederum mit analytischen Schätzungen abgeglichen werden. Bei niedrigen Geschwindigkeiten der Überströmung kann ein so genanntes "Pfeifen" beobachtet werden. Hierbei handelt es sich um ein Phänomen welches auftritt, wenn die Zeitskalen der Wirbel, die sich aufgrund der Überströmung am Hals des Resonators ablösen und auf der gegenüberliegenden Wand auf treffen, mit der Eigenfrequenz des Resonators übereinstimmen und periodische Druckfluktuationen verursachen. Dieser Effekt wird anschließend analytisch untersucht und mit einer kritischen Strouhal Zahl in Verbindung gebracht. Mithilfe von experimentell ermittelten Daten können die Simulationsergebnisse bis zu einer Überströmungsgeschwindigkeit von Mach 0,4 validiert werden, wobei auch teils eine größere Übereinstimmung als in anderen Veröffentlichungen festgestellt wird.

Contents

Nomenclature	ix
1 Introduction to Helmholtz Resonators	1
2 Overview on the Fundamentals of Fluid Mechanics and Acoustics	4
2.1 General Transport Equations	4
2.2 The Conservation Equations of Fluid Mechanics	5
2.3 Acoustics	7
3 Functional Principle of the Helmholtz Resonator	10
3.1 Wall Impedance of a Helmholtz Resonator	10
3.2 Estimation of the Eigenfrequency	11
3.3 Methods for Determination of the Wall Impedance	12
3.3.1 Impedance Tube Method	13
3.3.2 In Situ Method	14
3.4 Whistling Phenomenon	16
4 Test Case Geometry and Numerical Setup	17
4.1 Test Case Geometry	17
4.2 Meshes	17
4.3 Numerical Setup	20
5 Results of the Numerical Simulations	23
5.1 The Physics of Helmholtz Resonators with Grazing Flow	23
5.2 Hersh Helmholtz Resonator Cases	26
5.2.1 Comparison of the Experimental and the Simulation Results	28
5.2.2 Analysis of the Simulation Results with Grazing Flow	31
5.2.3 Numerical Simulation Results of the Whistling Phenomenon	33
5.3 Jones Helmholtz Resonator Case	36
5.3.1 Jones Experimental and Simulation Results with Grazing Flow	38
5.4 Evaluation of the In Situ Method	40
6 Summary and Conclusion	42
Appendices	44

CONTENTS

A Implementation of the In Situ Method in Matlab	45
B Calculation of Probe Coordinates in Matlab	47
Bibliography	51

Nomenclature

Roman Symbols

$\hat{\mathbf{e}}$	Directional vector of unit length	[-]
\hat{f}	Fourier coefficient of impinging pressure wave	[m/s]
\hat{g}	Fourier coefficient of reflected pressure wave	[m/s]
\hat{p}'	Fourier transforms of the fluctuating pressure	[Pa]
\hat{u}'	Fourier transforms of the fluctuating wall normal velocity	[m/s]
\mathbf{F}	Force	[N]
\mathbf{f}	Volumetric forces	[N/kg]
\mathbf{F}_K	Body forces	[N]
\mathbf{k}	Wave vector	[rad/m]
\mathbf{n}	Surface normal vector	[-]
\mathbf{P}	Impulse	[N s]
\mathbf{q}	Specific heat flux	[J/m ² s]
\mathbf{v}	Velocity	[m/s]
\mathbf{v}'	Fluctuating velocity	[m/s]
\mathbf{v}_0	Mean velocity	[m/s]
\mathbf{x}	Location	[m]
ρ	Density	[kg/m ³]
ρ'	Fluctuating density	[kg/m ³]
ρ_0	Mean density	[kg/m ³]

CONTENTS

M	Mach number	[-]
Pr	Prandtl number	[-]
St_{crit}	Critical Strouhal number	[-]
\tilde{E}	Energy (Lagrangian approach)	[J]
\tilde{S}	Integration boundary surface (Lagrangian approach)	[m ²]
\tilde{V}	Material volume (Lagrangian approach)	[m ³]
A	Amplitude	[Pa]
a, b	Integration limits	[m]
A_{fp}	Faceplate area	[m ²]
A_{th}	Throat area	[m ²]
c	Damping constant	[kg/s]
c_0	Speed of sound	[m/s]
d_0	Throat diameter	[m]
d_2	Inner diameter of a hexagon	[m]
E	Volume specific energy	[J/m ³]
e	Mass specific energy	[J/kg]
f	Impinging pressure wave	[m/s]
f_{eig}	Eigenfrequency	[Hz]
f_w	Whistling frequency	[Hz]
g	Reflected pressure wave	[m/s]
H	Height of the backing volume	[m]
h	Mass specific enthalpy	[J/kg]
h_{ch}	Channel height	[m]
k	Spring constant	[N/m]
l_0	Throat length	[m]
l_s	Channel length in stream direction	[m]

l_{cav}	Cavity length	[m]
l_{ch}	Channel length	[m]
l_e	Effective throat length	[m]
$l_{\text{s,corr}}$	Correction length	[m]
m	Mass	[kg]
p	Pressure	[Pa]
p'	Fluctuating pressure	[Pa]
p_+	Incident pressure wave	[Pa]
p_-	Reflected pressure wave	[Pa]
p_0	Mean pressure	[Pa]
p_a	Pressure at the frontplate	[Pa]
p_b	Pressure at the backplate	[Pa]
R	Reflection coefficient	[-]
r_0	Throat radius	[m]
r_{cav}	Cavity radius	[m]
R_l	Linear resistance term	[kg/s]
r_{min}	Minimum radius for pressure probe placement	[m]
R_{nl}	Non-linear resistance term	[kg/s]
S	Integration boundary surface	[m ²]
s	Correction factor	[-]
t	Time	[s]
U	Grazing flow velocity	[m/s]
u_a	Velocity at the frontplate	[m/s]
V	Volume	[m ³]
V_{cav}	Cavity volume	[m ³]
Z	Impedance	[Pa s/m]

CONTENTS

z Normalized impedance [-]

Greek Symbols

$\acute{\mu}$ Resistance against compression [-]

δ Kronecker delta [-]

κ Heat capacity ratio [-]

μ Dynamic viscosity [kg/m s]

ν Kinematic viscosity [m²/s]

ω Angular frequency [rad/s]

ω_{eig} Angular eigenfrequency [rad/s]

ϕ Phase angle [rad]

ψ Arbitrary fluid property [-]

σ Porosity [-]

τ Shear stress [N/mm²]

Other Symbols

$\angle R$ Phase of reflection coefficient [rad]

Acronyms

CFD Computational fluid dynamics

DFT Discrete Fourier Transformation

FV Fluid volume

NSCBC Navier-Stokes characteristics boundary condition

RTT Reynolds transport theorem

SPL Sound pressure level

1 Introduction to Helmholtz Resonators

An acoustic resonator is a device, used with the main purpose to dampen acoustic pressure fluctuations. There are several resonator types to achieve this goal, like Helmholtz resonators or quarter wave resonators, with this work focusing on the investigation and simulation of Helmholtz resonators and the effects of grazing flow. A Helmholtz resonator is a passive sound absorber, named after Hermann von Helmholtz, who was the first person to study its functional principles in detail [19]. Figure 1.1 depicts the basic geometry of such a resonator, with the incoming and reflected acoustic waves f and g traveling along a channel. The resonator cavities are separated from the channel by a faceplate covered in holes. Those holes are called the throat or neck of the resonator.

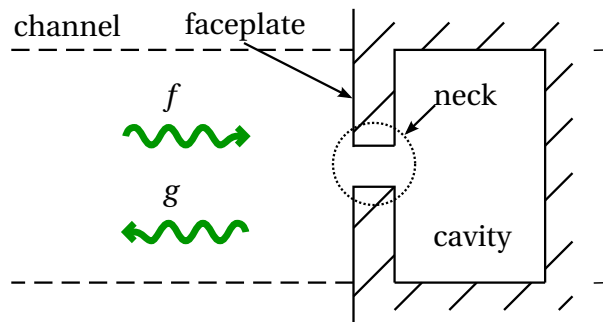


Figure 1.1: Generic sketch of a Helmholtz resonator.

The gas inside the cavity is compressed by an impinging pressure perturbation, causing the gas mass inside the neck to oscillate. There are various linear and non linear energy dissipation mechanisms, which in turn dampen the reflected acoustic wave. This will be explained further in Chapter 3 .

Helmholtz resonators are utilized in various applications, with a big part of the research taking place in the aerospace industry, where the development towards higher performance solutions is making a deep theoretical understanding of the functional principle of these type of acoustic dampeners necessary.

One application is the noise reduction in turbofan engines. Here, so-called acoustic liners are utilized on the inside of the engine cowling to dampen the noise that is being created by the core engine and the fan blades. These liners, which are schematically depicted in Fig. 1.2(a) consist of a panel of hexagonal cavities, covered by a thin perforated sheet and form an array of Helmholtz resonators.

Acoustic dampeners are also used in rocket engines, where thermoacoustic instabilities, created during the combustion process can damage or sometimes destroy the engine. One

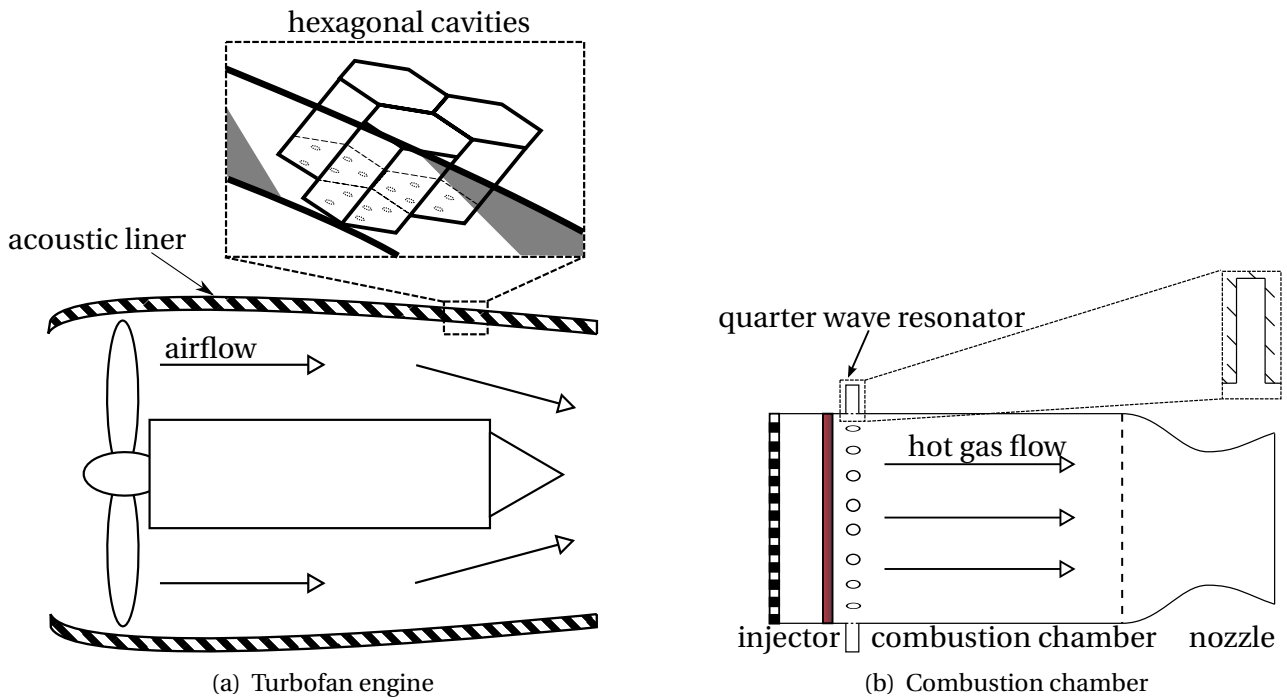


Figure 1.2: Generic sketch of a turbofan engine and combustion chamber.

method to avoid this effect, is to place a ring of resonator elements into the wall of the combustion chamber. This principle is depicted in Fig. 1.2(b) and further investigated by Förner et al. [7]. In this particular case, quarter wave resonators are used. This type of resonator consists of a tube, which is quarter of a wavelength long, based on the frequency which is to be dampened.

In both of the previously mentioned examples, the incident acoustic waves are coupled with a grazing flow, which is approximately parallel to the opening of the resonator. As this can have a massive influence on the performance characteristics of the resonator, it has been the subject of numerous studies.

The goal of this thesis is to set up a numerical simulation of a Helmholtz resonator under the influence of grazing flow, using OpenFOAM. The geometric dimensions are taken from experiments conducted by Hersh et al. [10] and Jones et al. [12]. Here, a particular interest lies in the accuracy of scaling methods, which are needed to simplify the hexagonal-cavity multi-throat configuration into a cylindrical-cavity single-throat configuration, while maintaining the impedance of the resonator. Another goal is to compare different impedance determination methods, namely the impedance tube and the in situ method. The simulation results are validated by comparing them to rough analytical calculations and experimental results.

The thesis is organized as follows. First Chapter 2 lays the theoretical groundwork needed to understand and solve the problems of fluid mechanics and acoustics that are encountered when dealing with Helmholtz resonators. After that, the concept of wall impedance and the mass-spring-dampener model will be used in Chapter 3 to explain the functional principle of a Helmholtz resonator. As determining the correct resonator impedance is crucial for analyz-

ing its performance, two methods for impedance measurement will be presented in Sec. 3.3 . In some cases a grazing flow over a cavity opening can result in a whistling phenomenon, similar to blowing over the neck of a bottle. This was encountered during the numerical simulations, so the theory behind the whistling phenomenon is presented in Sec. 3.4 before presenting the simulation results in Sec. 5.2.3 . Chapter 4 explains the numerical set up that was used to perform the simulations. Here, the geometry of the test cases is presented, along with details about the meshing.

Numerous numerical simulations with varying frequencies, sound pressure levels and grazing flow Mach numbers were performed. The results of these are presented and discussed in Chapter 5 . The results are then further compared to experiments performed by Hersh et al. [10] and Jones et al. [12].

2 Overview on the Fundamentals of Fluid Mechanics and Acoustics

This chapter gives a quick overview and summary on the fundamental equations of fluid mechanics. The theory used in this section is based on the fluid mechanics-I script by Adams [3].

2.1 General Transport Equations

The Material Derivative

The rate of change of a fluid property ψ at a location \mathbf{x} and time t is caused by:

- a change $\partial\psi/\partial t$ in an individual fluid element
- different fluid elements passing \mathbf{x} as time progresses

To describe those effects mathematically, the material derivative D/Dt is introduced. Using $\mathbf{v}(\mathbf{x}, t)$ as the velocity vector, it is defined as:

$$\frac{D\psi}{Dt} = \frac{\partial\psi}{\partial t} + (\mathbf{v} \cdot \nabla)\psi . \quad (2.1)$$

The first term on the right is the local derivative and the second one is called the convective derivative.

The Reynolds Transport Theorem

The Reynolds transport theorem (RTT) describes the rate of change of a chosen fluid property for a distinct fluid volume (FV) \tilde{V} . The tilde sign marks that the FV is being followed by the spectator (Lagrangian approach), rather than focusing on a specific location (Eulerian approach).

To describe the time derivative of an arbitrary function $f(x, t)$ in one spacial dimension, with the time dependent integration limits $a(t)$ and $b(t)$, the Leibniz-Theorem is introduced:

$$\frac{d}{dt} \int_{a(t)}^{b(t)} f(x, t) dx = \int_{a(t)}^{b(t)} \frac{\partial f}{\partial t} dx + f(b, t) \frac{db}{dt} - f(a, t) \frac{da}{dt} . \quad (2.2)$$

Here, the first term on the right hand side describes the change of the function itself, while the following terms take the changing integration limits into account. The terms da/dt and db/dt can be interpreted as the velocity \mathbf{v} of the integration limits.

Equation (2.2) can now be formulated for a three dimensional FV with the boundaries $S(t)$ and for the arbitrary fluid property $\psi(\mathbf{x}, t)$

$$\frac{d}{dt} \int_{V(t)} \psi(\mathbf{x}, t) dV = \int_{V(t)} \frac{\partial \psi}{\partial t} dV + \int_{S(t)} \psi \mathbf{v}_s \cdot \mathbf{n} dS. \quad (2.3)$$

Using the divergence theorem, the surface integral on the right-hand side of Eq. (2.3) can be rewritten as a volume integral, which leads to the final form of the Reynolds transport theorem:

$$\frac{d}{dt} \int_{V(t)} \psi(\mathbf{x}, t) dV = \int_{V(t)} \left(\frac{\partial \psi}{\partial t} + \nabla(\psi \cdot \mathbf{v}) \right) dV. \quad (2.4)$$

2.2 The Conservation Equations of Fluid Mechanics

Conservation of Mass

The continuity equation states that the mass m in a material fluid volume \tilde{V} stays constant. Mathematically, this statement can be expressed as follows:

$$\frac{dm}{dt} = \frac{d}{dt} \int_{\tilde{V}} \rho(\mathbf{x}, t) dV = 0. \quad (2.5)$$

Using the RTT from Eq. (2.4) and exchanging the arbitrary property $\psi(\mathbf{x}, t)$ by the density $\rho(\mathbf{x}, t)$, the integral form of the continuity equation is found:

$$\frac{dm}{dt} = \int_V \left(\frac{\partial \rho}{\partial t} + \nabla(\rho \cdot \mathbf{v}) \right) dV = 0. \quad (2.6)$$

Equation (2.6) is independent of the chosen volume and can therefore be rewritten to obtain its differential form

$$\frac{\partial \rho}{\partial t} + \nabla(\rho \cdot \mathbf{v}) = 0. \quad (2.7)$$

Conservation of Momentum and the Navier-Stokes Equations

Newtons second law formulated for a material FV \tilde{V} states that the time derivative of the impulse \mathbf{P} of said volume is equal to the sum of all forces \mathbf{F}_m acting upon it

$$\frac{d\mathbf{P}}{dt} = \frac{d}{dt} \int_{\tilde{V}} \rho \mathbf{v} dV = \sum_m \mathbf{F}_m. \quad (2.8)$$

Here, the product $\rho \mathbf{v}$ can be associated with the property $\psi(\mathbf{x}, t)$. Using Eq. (2.4) yields the integral form of the momentum equation

$$\int_V \left(\frac{\partial \rho \mathbf{v}}{\partial t} + \nabla(\rho \mathbf{v} \cdot \mathbf{v}) \right) dV = \int_V (-\nabla p + \nabla \tau + \rho \mathbf{f}) dV + \mathbf{F}_K. \quad (2.9)$$

The terms on the right-hand side of Eq. (2.9) represent the various types of forces that can act upon a fluid volume.

2.2 The Conservation Equations of Fluid Mechanics

- ∇p represents the pressure forces and $\nabla \tau$ represents the normal and shear stresses acting upon a surface \tilde{S} .
- \mathbf{f} represents the volumetric forces, that may act upon every fluid element in \tilde{V} .
- \mathbf{F}_K represents the body forces that may act upon specific points of the volume \tilde{V} .

If no body forces act on the FV ($\mathbf{F}_K = 0$), Eq. (2.9) has to be valid independent of the chosen volume. This leads to the differential form of the momentum equation

$$\frac{\partial \rho \mathbf{v}}{\partial t} + \nabla(\rho \mathbf{v} \cdot \mathbf{v}) = -\nabla p + \nabla \tau + \rho \mathbf{f}. \quad (2.10)$$

Using Eq. (2.7) the left side of Eq. (2.10) can be rewritten,

$$\frac{\partial \mathbf{v}}{\partial t} + (\mathbf{v} \cdot \nabla) \mathbf{v} = -\frac{1}{\rho} \nabla p + \frac{1}{\rho} \nabla \tau + \mathbf{f} \quad (2.11)$$

Neglecting frictional forces ($\tau = 0$), Eq. (2.11) can be rewritten as the Euler Equation,

$$\frac{\partial \mathbf{v}}{\partial t} + (\mathbf{v} \cdot \nabla) \mathbf{v} = -\frac{1}{\rho} \nabla p + \mathbf{f}. \quad (2.12)$$

The starting point of the Navier-Stokes equations is the momentum equation (2.11), with the shear stress tensor τ expressed in dependence of the acceleration $\partial v_i / \partial v_j$ and the dynamic viscosity μ of the flow.

Assuming a Newtonian fluid, the stress tensor τ is stated by Kundu et al. [14] to be:

$$\tau_{ij} = \mu \left(\frac{\partial v_i}{\partial x_j} + \frac{\partial v_j}{\partial x_i} - \frac{2}{3} \delta_{ij} \frac{\partial v_k}{\partial x_k} \right) + \hat{\mu} \delta_{ij} \frac{\partial v_k}{\partial x_k}. \quad (2.13)$$

Here, δ is the Kronecker delta ($\delta_{ij} = 1$ for $i = j$ and $\delta_{ij} = 0$ for $i \neq j$) and $\hat{\mu}$ is the resistance against compression. Using the Stokes Hypothesis, sets $\hat{\mu} = 0$ and inserting Eq. (2.13) into the previously mentioned momentum equation, leads to the Navier-Stokes equations:

$$\frac{\partial \mathbf{v}}{\partial t} + (\mathbf{v} \cdot \nabla) \mathbf{v} = -\frac{1}{\rho} \nabla p + \frac{\mu}{\rho} \left(\Delta \mathbf{v} + \frac{1}{3} \nabla(\nabla \cdot \mathbf{v}) \right). \quad (2.14)$$

Conservation of Energy

The time derivative of the energy \tilde{E} , with the tilde sign signifying that the FV \tilde{V} is being followed by the spectator, is equal to the sum of the powers that are exerted by the acting forces and additionally to the sum of the in- and outflow of heat. Note that E is the volume specific energy, which is \tilde{E}/V :

$$\frac{d\tilde{E}}{dt} = \frac{d}{dt} \int_{\tilde{V}} E dV = \sum (\text{power} + \text{heat-flux}). \quad (2.15)$$

Keeping with the same principle as in the previous section, Eq. (2.4) is used to further expand Eq. (2.15) :

$$\int_V \left(\frac{\partial E}{\partial t} + \nabla \cdot (E\mathbf{v}) \right) dV = \int_V (-\nabla \cdot (p\mathbf{v}) + \nabla \cdot (\boldsymbol{\tau} \cdot \mathbf{v}) + \rho \mathbf{f} \cdot \mathbf{v} - \nabla \cdot \mathbf{q}) dV . \quad (2.16)$$

Here, the terms on the right-hand side of Eq. (2.16) have the following meaning:

- $\nabla \cdot (p\mathbf{v})$: power generated by expansion
- $\nabla \cdot (\boldsymbol{\tau} \cdot \mathbf{v})$: power generated by the surface and shear tension
- $\rho \mathbf{f} \cdot \mathbf{v}$: power generated by the volumetric forces
- \mathbf{q} : heat-flux vector

Again the equation above has to be valid for any chosen Volume and can therefore be rewritten in the following form:

$$\frac{\partial E}{\partial t} + \nabla \cdot (E\mathbf{v}) = -\nabla \cdot (p\mathbf{v}) + \nabla \cdot (\boldsymbol{\tau} \cdot \mathbf{v}) + \rho \mathbf{f} \cdot \mathbf{v} - \nabla \cdot \mathbf{q} . \quad (2.17)$$

Neglecting body forces ($\mathbf{f} = \mathbf{0}$) and introducing the enthalpy with the mass specific energy e defined as E/ρ

$$h = e + \frac{p}{\rho} , \quad (2.18)$$

Equation (2.17) can be transformed further:

$$\rho \frac{Dh}{Dt} = \frac{Dp}{Dt} + \nabla \cdot \boldsymbol{\tau} \cdot \mathbf{v} - \nabla \cdot \mathbf{q} . \quad (2.19)$$

2.3 Acoustics

Acoustics is the study of disturbances of flow variables that are small compared to their mean value. The acoustic quantities that are studied, are the pressure p , the density ρ , and the velocity \mathbf{v} . In general, the mean values are constant and orders of magnitude larger than the disturbances, which fluctuate in time and space. The theory used in this section is based on Ehrenfried [6] and Polifke et al. [16].

If ψ represents the total value of an arbitrary quantity with the mean value ψ_0 , then its fluctuation can be expressed with $\psi'(\mathbf{x}, t)$, leading to the following expressions:

$$p(\mathbf{x}, t) = p_0 + p'(\mathbf{x}, t) \quad (2.20)$$

$$\rho(\mathbf{x}, t) = \rho_0 + \rho'(\mathbf{x}, t) \quad (2.21)$$

$$\mathbf{v}(\mathbf{x}, t) = \mathbf{v}_0 + \mathbf{v}'(\mathbf{x}, t) . \quad (2.22)$$

Those expressions can now be inserted into the continuity equation (2.7) and the Euler equation (2.12) to obtain their respective acoustic counterparts:

$$\frac{\partial \rho'}{\partial t} + \rho_0 \nabla \cdot \mathbf{v}' = 0 \quad (2.23)$$

$$\rho_0 \frac{\partial \mathbf{v}'}{\partial t} + \nabla p' = 0. \quad (2.24)$$

The Wave Equation

Before deriving the wave equation, an expression for $p(\mathbf{x}, t) = p(\rho)$ has to be found. At constant entropy s , the pressure p is found to be a function of density only. By performing a Taylor expansion of p around ρ_0 with respect to ρ , the following expression is found:

$$p' = c_0^2 \rho'. \quad (2.25)$$

Here, the speed of sound is introduced:

$$c_0 = \sqrt{\gamma RT} = \sqrt{\gamma \frac{p}{\rho}}. \quad (2.26)$$

Note that Eq. (2.26) is only valid for an ideal gas. Now, Eq. (2.25) can be inserted into Eq. (2.23) to get:

$$\frac{1}{c_0^2} \frac{\partial p'}{\partial t} + \rho_0 \nabla \cdot \mathbf{v}' = 0. \quad (2.27)$$

After calculating the divergence of Eq. (2.23) and subtracting it from the time derivative of Eq. (2.27), the wave equation for pressure disturbances is obtained:

$$\frac{\partial^2}{\partial t^2} p' - c_0^2 \Delta^2 p' = 0. \quad (2.28)$$

Solution of the Wave Equation

A general solution of Eq. (2.28) for one dimension is expressed by using the two arbitrary functions f and g , with the simplification that the disturbances are traveling in x_1 direction only:

$$\frac{p'(x_1, t)}{\rho c_0} = f(x_1 - c_0 t) + g(x_1 + c_0 t). \quad (2.29)$$

The validity of this solution can be easily verified by inserting Eq. (2.29) into Eq. (2.28).

Along the eigenmodes of the wave problem, the f and g waves stay constant and are called Riemann invariants, which can be expressed in terms of p' and v' :

$$\begin{aligned} f &= \frac{1}{2} \left(\frac{p'}{\rho c_0} + v'_1 \right) \\ g &= \frac{1}{2} \left(\frac{p'}{\rho c_0} - v'_1 \right). \end{aligned} \quad (2.30)$$

The f and g waves are traveling in positive and negative x_1 directions, respectively.

To obtain the general solution for the wave equation in a multi-dimensional case, Eq. (2.29) can be written as:

$$\frac{p'(\mathbf{x}, t)}{\rho c_0} = f(\hat{\mathbf{e}} \cdot \mathbf{x} - c_0 t) + g(\hat{\mathbf{e}} \cdot \mathbf{x} + c_0 t), \quad (2.31)$$

with $\hat{\mathbf{e}}$ being a directional vector with unity length.

For harmonic waves, a solution for Eq. (2.31) can be found as

$$p'(\mathbf{x}, t) = A \exp(j\omega t - j\mathbf{k} \cdot \mathbf{x}), \quad (2.32)$$

with ω as the fixed angular frequency, A as the wave amplitude and the wave vector

$$\mathbf{k} = \hat{\mathbf{e}} \frac{\omega}{c_0}. \quad (2.33)$$

3 Functional Principle of the Helmholtz Resonator

The behavior of a Helmholtz resonator is often described using the model of a mass-spring damper system, as depicted in Fig. 3.1. In this model, the mass m in the neck of the resonator is taking part in the oscillation, while the spring constant k can be associated with the compressibility of the air in the backing volume. As mentioned i.a. by Förner et al. [8], the losses of the incoming sound wave, represented by the viscous damping coefficient c , are caused by linear and non linear energy dissipation mechanisms:

- For sound low pressure levels (SPL), the dissipation is mainly caused by a linear mechanism. As the air volume in the neck is oscillating, energy is dissipated by friction of the flow with the neck wall.
- As the SPL is increased, non-linear mechanisms dominate as a cause for dissipation of acoustic energy. As the velocity of the flow in the neck increases, the flow separates at the neck of the resonator and vortices are formed. This increases the energy dissipation considerably, as major parts of the acoustic energy is transferred into turbulent perturbation of the fluid.

3.1 Wall Impedance of a Helmholtz Resonator

To describe the dynamic behavior of a Helmholtz resonator, the surface impedance $Z(\omega)$ is defined for a given angular frequency ω , where \hat{p}' and \hat{u}' are the Fourier transforms of the fluctuating pressure and wall normal velocity:

$$Z(\omega) = \frac{\hat{p}'(\omega)}{\hat{u}'(\omega)}. \quad (3.1)$$

The acoustic impedance should be considered as an apparent property of the resonator, making it an effective boundary condition for the incident acoustic field, when it impinges upon the surface as stated by Zhang [20]. With this definition, Z can be interpreted as a transfer function from \hat{u} to \hat{p} , which is only valid in the linear regime. At higher SPLs, the impedance cannot be described by a linear function anymore, as it changes with the amplitude of the signal.

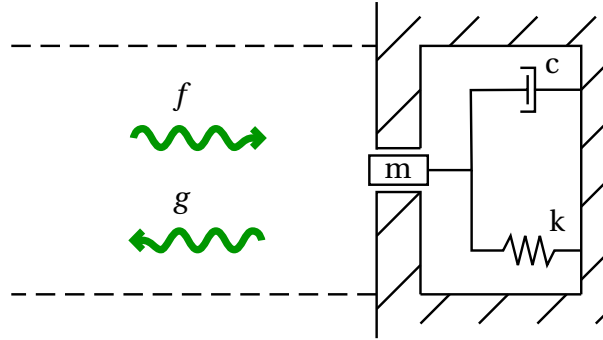


Figure 3.1: Mass-spring dampener model.

The mass spring model can be expressed using the following equation:

$$Z(\omega) = R_l + R_{nl} + j \left(m\omega - \frac{k}{\omega} \right). \quad (3.2)$$

The real and imaginary parts of Z are called the resistance and reactance, respectively. The losses are represented by the linear and non-linear resistance terms R_l and R_{nl} .

In the following chapters and figures, the normalized impedance z will be used:

$$z = \frac{Z}{\rho_0 c_0}. \quad (3.3)$$

The purpose of an acoustic liner is to dampen an oncoming pressure wave f and to reflect a wave g at a lower amplitude. This effect is expressed with the reflection coefficient R

$$R(\omega) = \frac{\hat{g}(\omega)}{\hat{f}(\omega)}, \quad (3.4)$$

with \hat{f} and \hat{g} being the Fourier coefficients of the f and g wave. The damping efficiency can be judged by considering the gain of the reflection coefficient. Its phase $\angle R$ describes the phase difference of the f and g wave at the reference position.

Taking the definition of f and g from Eq. (2.30) and of the reflection coefficient R from Eq. (3.4), the impedance z can be expressed as a function of the reflection coefficient and therefore f and g :

$$z = \frac{1 + R}{1 - R}. \quad (3.5)$$

3.2 Estimation of the Eigenfrequency

In order to find an expression for the eigenfrequency of a Helmholtz resonator, it is useful to look at the definition of the eigenfrequency ω_{eig} for a mass-spring-damper system:

$$\omega_{\text{eig}} = \sqrt{\frac{k}{m}}. \quad (3.6)$$

3.3 Methods for Determination of the Wall Impedance

Following both Keller and Zauner [13] as well as Garrison et al. [9], the compressibility constant c and the oscillating mass m can be determined with the following equations

$$\begin{aligned} m &= (1 + s)l_e\rho_0 \\ k &= \frac{A_{\text{th}}\rho_0 c_0^2}{V_{\text{cav}}} \end{aligned} \quad (3.7)$$

Here, s is a correction factor that contains various boundary layer effects, A_{th} is the throat area and V_{cav} is the cavity volume.

$$s = \left(1 + \frac{\kappa - 1}{\sqrt{\text{Pr}}}\right) \frac{\sqrt{2\nu/\omega}}{d_0}, \quad (3.8)$$

where κ , Pr , ν and d_0 denote the heat capacity ratio, Prandtl number, kinematic viscosity and throat diameter. One important parameter for determining eigenfrequency of the system is the effective throat length $l_e = l_0 + l_{\text{s,corr}}$, consisting of the throat length l_0 and a correction length $l_{\text{s,corr}}$. The reasoning behind this correction is, that not only the gas directly inside the neck takes part in the oscillation, but also a certain amount of gas before and after the neck opening, increasing the effective oscillating mass.

With Eq. (3.7) inserted into Eq. (3.6), the eigenfrequency can be expressed as

$$\omega_{\text{eig}} = c \sqrt{\frac{A_{\text{th}}}{V_{\text{cav}}(1 + s)l_e}}. \quad (3.9)$$

There are several correlations available to determine the correction length l_s , this work will only concentrate on two. The first method by Ingard [11] is recommended for large aspect ratio resonators ($(d_0/\sqrt[3]{V}) \ll 1$) and specifies $l_{\text{s,corr}}$ as

$$l_{\text{s,corr}} = \frac{8}{3\pi} d_0. \quad (3.10)$$

While this method gives reasonable accurate results in most cases, it does not account for changes in the resonance frequency due to grazing flow at varying Mach numbers M . This effect is included in the model set up by Rice [17], which states that

$$l_{\text{s,corr}} = \frac{0.85d_0(1 - 0.7\sqrt{\sigma})}{1 + 305M^3}. \quad (3.11)$$

Here, σ is the porosity, which is defined in Eq. (4.1).

3.3 Methods for Determination of the Wall Impedance

Ideally the wall impedance is determined by calculating $Z = \hat{p}'/\hat{u}'$, using measurements of p and u at a reference plane, located at a far enough distance from the resonator as not to be influenced by turbulent pressure fluctuations. In experiments it is difficult to obtain such

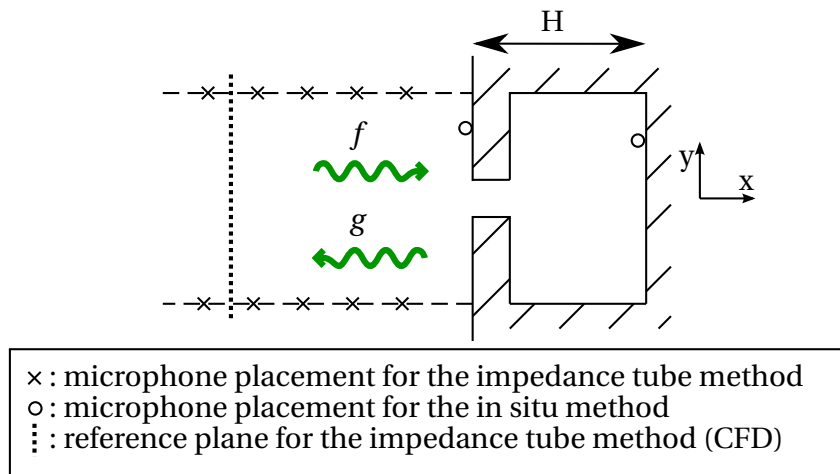


Figure 3.2: Impedance tube method and in situ method.

measurements, as the sensors have to be flush mounted to the channel wall, to not interact with the flow and it is quite challenging to obtain the acoustic fluctuating velocity u' directly.

In order to determine Z in an experimental setup, several methods have been devised, which only require wall mounted microphones. The two methods presented in the following chapters are the impedance tube method, which uses microphones mounted in the channel, followed by the in situ method, with microphones mounted on the frontplate and backplate of the resonator.

3.3.1 Impedance Tube Method

The impedance tube method is typically used to determine the impedance of acoustic dampening elements. Its basic principle is depicted in Fig. 3.2 and involves pressure measurements on several positions along the resonator channel. There are various implementations of this method, depending on the experimental buildup. Jones et al. [12] uses 95 microphones flush mounted inside the channel. To determine the impedance of the resonator, the complex pressure measurements have to be solved iteratively.

Here, one advantage of a numerical simulation shows up, as the fluctuating pressure p' and velocity u' can be determined directly without disturbing the flow field. Implementing this method, the pressure and velocity fluctuations are measured at a reference plane, that is distant enough from the resonator faceplate to not be disturbed by any turbulent fluctuations. Furthermore, the mean data can be determined for the whole plane at once, instead of using individual sensor measurements on the channel wall. This information can then be used in the post-processing to directly calculate the f and g wave from Eq. (2.30). The reflection coefficient can afterwards be calculated using Eq. (3.4) to obtain the impedance Z with Eq. (3.5). Using the real and imaginary parts of z , the resistance and reactance can be easily determined as seen i.a. in Förner [8].

3.3.2 In Situ Method

This section describes a method to obtain the impedance Z using only two microphones, located on the frontplate and the backplate of the resonator.

Starting with Eq. (3.3), the impedance Z can be expressed using

$$Z = \frac{p_a}{u_a}, \quad (3.12)$$

with p_a and u_a as the pressure and velocity of the fluid at the frontplate.

The principle idea of the in situ method, which is thoroughly discussed by Dean [5], is to solve Eq. (3.12) by measuring the pressure p_a on the frontplate and calculating u_a , using the pressure p_b on the backplate of the cavity.

In order to obtain a useful result, following assumptions are made:

- Wave motion is in x -direction only.
- The cavity walls are sufficiently massive, so that no transmission is occurring perpendicular to the x -direction .
- A wave entering the cavity is totally reflected by the back wall.
- The faceplate is assumed as acoustically thin, making the particle velocity on both sides of the faceplate identical.

With these assumptions and Eq. (2.32) the incident (p_+) and reflected (p_-) pressure wave can be expressed as

$$\begin{aligned} p_+ &= p_0 \exp(j\omega t - j kx) \\ p_- &= p_0 \exp(j\omega t + j kx) . \end{aligned} \quad (3.13)$$

By adding the incident and reflected pressure waves, the formula for the standing wave can be determined. With $2p_0 = p_b$ this leads to the following form

$$p' = p_b \exp(j\omega t) \cos kx . \quad (3.14)$$

Now with Eq. (2.24) the acoustic particle velocity inside the cavity can be calculated as

$$u' = -j \frac{p_b}{\rho c_0} \exp(j\omega t) \sin kx . \quad (3.15)$$

Going back to the previous assumptions, the particle velocity inside the cavity on the backside of the frontplate, is assumed to be identical to the frontside of the frontplate. So with $x = H$ and inserting Eq. (3.15) into Eq. (3.12) leads to the final form of the impedance equation for the in situ method:

$$z = -j \frac{|\hat{p}_a|}{|\hat{p}_b|} \frac{e^{j\phi}}{\sin kH}, \quad (3.16)$$

Here, ϕ is phase angle between p_a and p_b , k is the axial wave number from Eq. (2.33) and H is the height of the backing volume. A sketch of the microphone placement, when implementing this method can be seen in Fig. 3.2.

The measurements done during the course of this work and also Zhang [20] showed, that using only two microphones would be problematic because of the difficulties separating the acoustic from the turbulent pressure fluctuations. To overcome this problem several sensors should be placed on both the faceplate and backplate, averaging their results in post-processing eliminates the turbulent fluctuations.

In order to minimize the amount of turbulent fluctuating pressure corrupting the measurements, the microphones on the frontplate should be placed at a minimum distance to the neck opening. The minimum distance depends heavily on the parameters of the experiment and on how much physical space is available, but should be in the region of at least several times the neck diameter ($r_{\min} \approx 3\text{--}10$ times d_0). The placement of the backplate sensors is less critical, as the turbulence caused at the neck has enough room to dissipate before reaching the backside of the cavity.

There is no specific rule for the number of sensors that should be used, the general rule being that more probes are needed for more turbulent flows and less probes are needed at the backplate to get smooth pressure data, because the pressure fluctuations are less turbulent there.

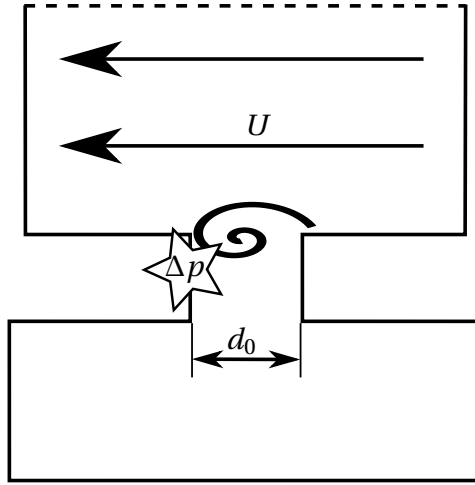


Figure 3.3: Mechanics of the whistling phenomenon.

3.4 Whistling Phenomenon

In the investigation of grazing flow over resonators, it is possible that under certain circumstances the fluid inside the resonator is excited at its eigenfrequency by the grazing flow itself, rather than by an incoming pressure wave. This effect is basically the same as when blowing over the neck of a water bottle. As this can result in some unexpected behavior of the resonator, it is important to be able to predict and understand this phenomenon.

According to Tonon et al. [18] this whistling phenomenon most likely occurs at a critical Strouhal number St_{crit} , which is defined as

$$St_{\text{crit}} = \frac{f_w d_0}{U} \quad \text{with } St_{\text{crit}} \in [0.38, 0.75] . \quad (3.17)$$

Here, f_w is the whistling frequency of the system, d_0 is the throat diameter and U is the velocity of the grazing flow. According to findings made by Binnie [4], St_{crit} depends on the throat diameter and can range from 0.38 to 0.75. Because the geometry that was investigated by Binnie [4] (simple rectangular cavities in a pipe system) differs from the resonator geometry discussed in this work, it is difficult to give an exact answer for the critical Strouhal number in this case.

Figure 3.3 depicts the basic mechanics that induce the whistling. The flow is unable to follow the edge of the resonator throat and a vortex forms, traveling across the opening of the resonator. The vortex that is reaching the opposite throat wall, produces a pressure spike Δp , which in turn causes another vortex to shed of the resonator throat. If the time scale of this effect coincides with the eigenfrequency of the resonator, which happens for a combination of certain flow velocities and throat diameters, than a periodical pressure fluctuation is generated as the mass in the resonator throat is oscillated.

4 Test Case Geometry and Numerical Setup

The following section explains in detail the notation used for describing the resonator geometry, before the meshing and numerical setup for the calculations is discussed. The 3D meshes were created using an icem script, that contained the geometrical dimensions and cell resolution of the mesh and allowed for simple creation of different resonator geometries. This mesh was transferred to an OpenFOAM compatible format, where the grazing flow speed, the boundary layer thickness as well as the frequency and the sound pressure level of the incident wave could be adjusted for investigation of different cases.

4.1 Test Case Geometry

The resonator geometry consists of a cylindrical cavity, a neck portion and a rectangular channel segment. The meaning of the various parameters is depicted in Fig. 4.1, with l_0 and r_0 being the length and diameter of the resonator neck and l_{cav} and r_{cav} denoting the length and diameter of the cavity, respectively. The faceplate geometry is defined by its length in y -direction l_s and in z -direction l_{ch} . The channel height is h_{ch} .

The porosity of the liner is expressed by σ , which can be calculated using

$$\sigma = \frac{nA_{\text{th}}}{A_{\text{fp}}}. \quad (4.1)$$

With n denoting the average number of holes per cavity and $A_{\text{th}} = r_0^2\pi$ and $A_{\text{fp}} = l_s l_{\text{ch}}$ representing the area of neck and faceplate, respectively.

4.2 Meshes

The mesh structure is a hybrid of a H-grid for the far field around the resonator and a O-grid for the area around the neck and can be separated into four main regions as seen in Fig. 4.2. Area I and IV are hexahedra-meshes with a relatively low resolution, because they are located at the far field around the resonator neck, where its influence is quite low. The resolution increases towards the central axis of the resonator, first in the midfield in area II and then close to the central axis in area III, which has the finest mesh resolution. Both areas are circular O-grids, designed to obtain the highest resolution in, and closely around the resonator neck. Figure 4.3 shows a top-view of the mesh, with regions I–III. In the zoomed perspective also a

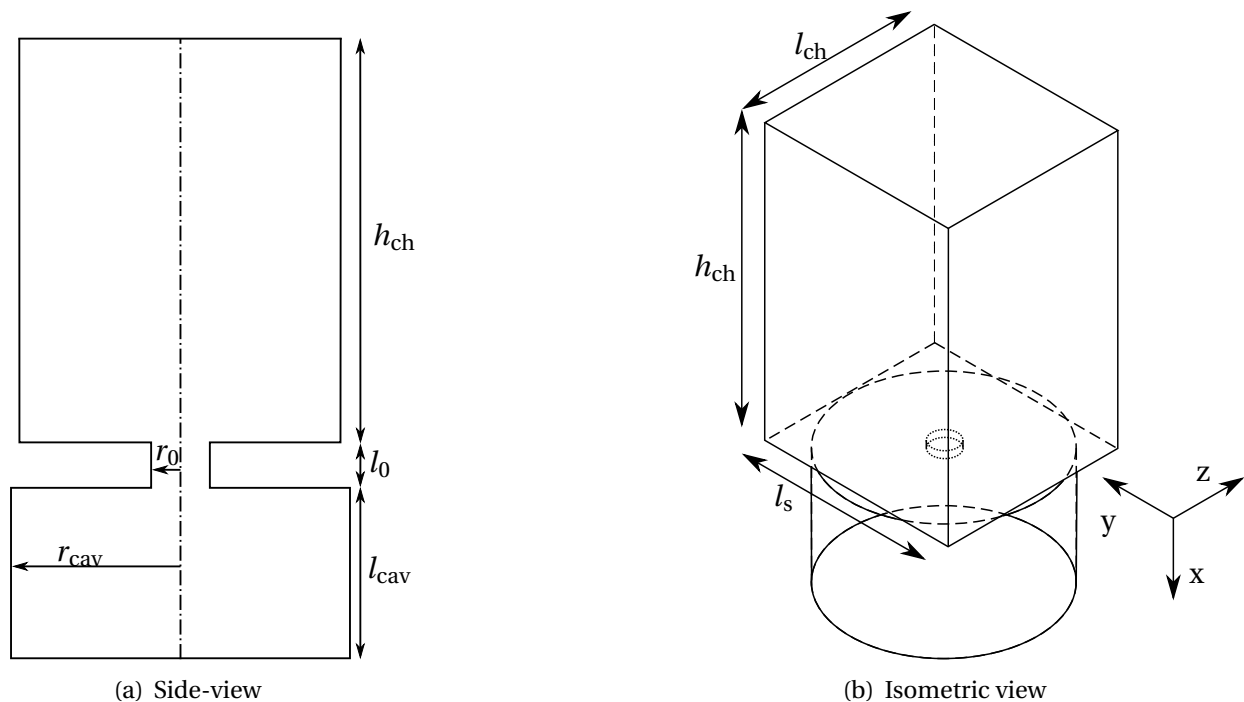


Figure 4.1: Sideview and isometric view of the resonator geometry.

region III_a is visible. This is an additional H-grid, which aims to remove the singularity that is encountered in the center of O-grids. The mesh in area V consists of rectangular cuboids. This was done to enable a smooth data transfer between the grid elements, if simulating multiple resonators in a grid. This is a potential task for the future and has not been done yet.

According to Förner et al. [8], it is important to choose the minimum cell size l_{\min} at the resonator neck small enough, in order to resolve the boundary layer correctly. The boundary layer thickness can be estimated using the Stokes length $\delta_s = 2\pi\sqrt{2\nu/\omega}$. Table 4.1 lists the total number of cells N , δ_s and minimum cell sizes l_{\min} for the two cases investigated in this work.

	N [10^6]	δ_s [10^{-5}m]	l_{\min} [10^{-5}m]
Hersh-mesh	3.48	46	2
Jones-mesh	3.35	25	1

Table 4.1: Mesh data for the Hersh and Jones cases.

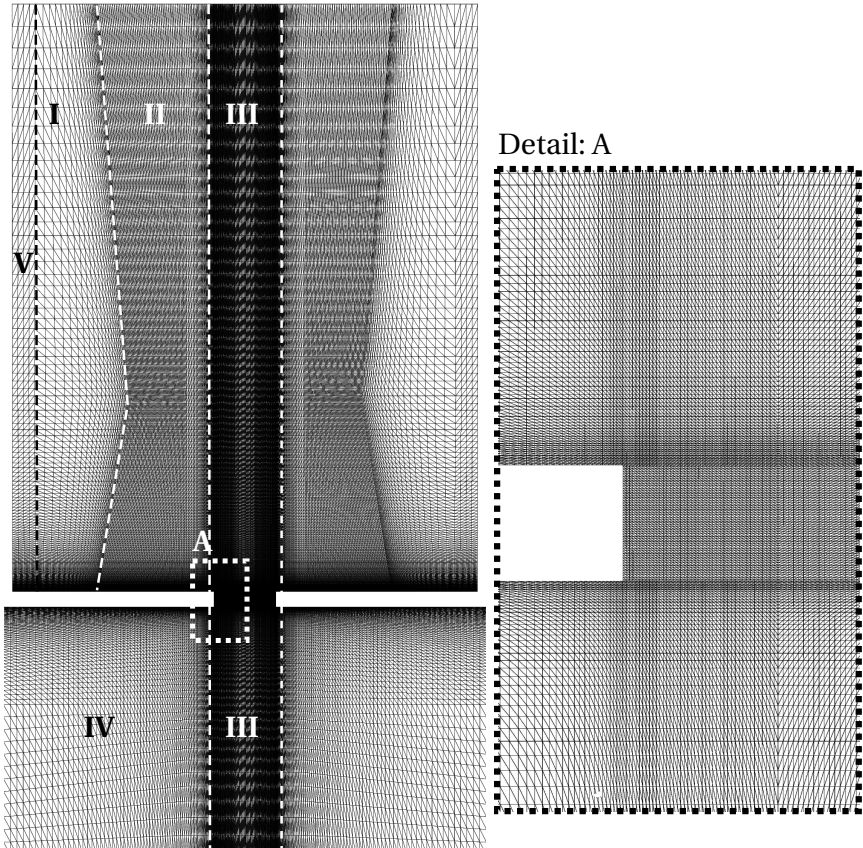


Figure 4.2: Side-view of the resonator mesh.

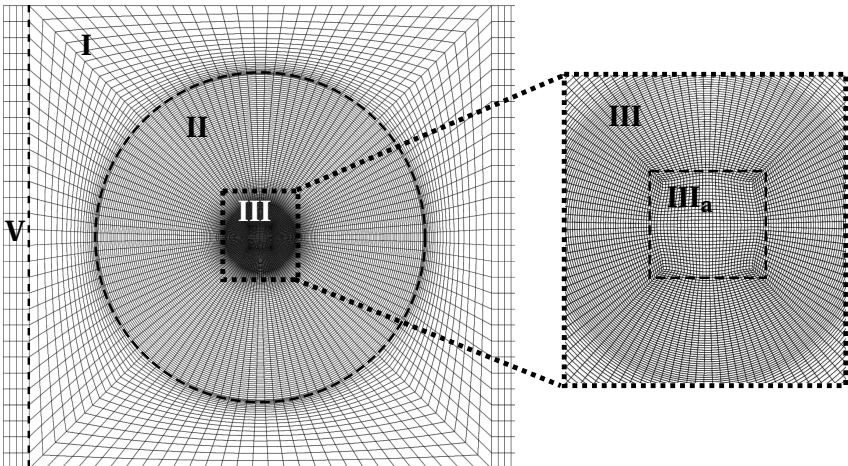


Figure 4.3: Top-view of the resonator mesh.

4.3 Numerical Setup

Open Source Field Operation and Manipulation, or short OpenFOAM, is a C++ library that provides tools and applications to solve various fluid mechanics problems. The solver used in the present study is the rhoPimpleFoam solver, provided by OpenFOAM. The annotations in the Code for the rhoPimpleFoam algorithm [1] state, that it is suited for applications with a transient, turbulent and compressible flow, as it is often the case with acoustic resonators. This solver utilizes the PISO SIMPLE algorithm [2], which solves the Navier Stokes equation for every cell and time step. The solver utilizes three nested loops, which are pictured in Fig. 4.4. The outermost loop is the temporal loop which is executed once every time step, until the last time step has been finished. Inside the temporal loop is the Pimple loop, which solves the discretized momentum equation, by guessing of the pressure field to obtain the velocity field components. Then it uses the velocity field components to compute the mass fluxes at the cell faces and solve the energy equation. Afterwards the PISO loop is entered, where the pressure equation is solved and the mass fluxes and velocities are corrected based on the new pressure field. The PISO algorithm is repeated two times, after which the Pimple loop is restarted until a preset convergence condition is reached, or until the Pimple loop has been repeated a maximum number of 22 times.

The boundary conditions used in the simulation are presented in Fig. 4.5 . The inlet and outlet plane, which are perpendicular to the y -axis, use a cyclic boundary condition, meaning that the fluid exiting the outlet plane, re-enters the inlet plane in the same state. The turbulent fluid movement caused by the resonator, is also carried over, which mimics to some degree the presence of additional resonators along the y -axis. Often multiple resonators are arranged on a liner, so this may lead to a more realistic simulation behavior. The excitation plane on top of the channel is configured with a Navier-Stokes characteristics boundary condition (NSCBC), which has been investigated by Poinot and Lele [15] and ensures low reflection of the outgoing g -wave. Further it has the functionality to impose a input wave continuously for every time step. In this study only sinusoidal input signals are considered. The walls perpendicular to the z -axis are configured with the slip condition, while the faceplate as well as the resonator walls have the no-slip boundary condition.

For the simulations with grazing flow, a simple laminar velocity profile was chosen. The profile can be seen in Fig. 4.6 for a Mach number of 0.1 . The shape of the profile itself is more of a rough approximation rather than being based on a real laminar flow profile. It was created by plotting a quadratic curve between the faceplate and a reference point, the boundary conditions being zero velocity at the wall and grazing flow velocity at the reference point. The boundary layer thickness was chosen as 1 mm for all cases, which may seem quite low compared to the actual boundary layer thickness, which is about one order of magnitude higher. The reasoning behind choosing such a small value is the improved visibility of interaction effects between the fluctuating flow in the neck and the grazing flow.

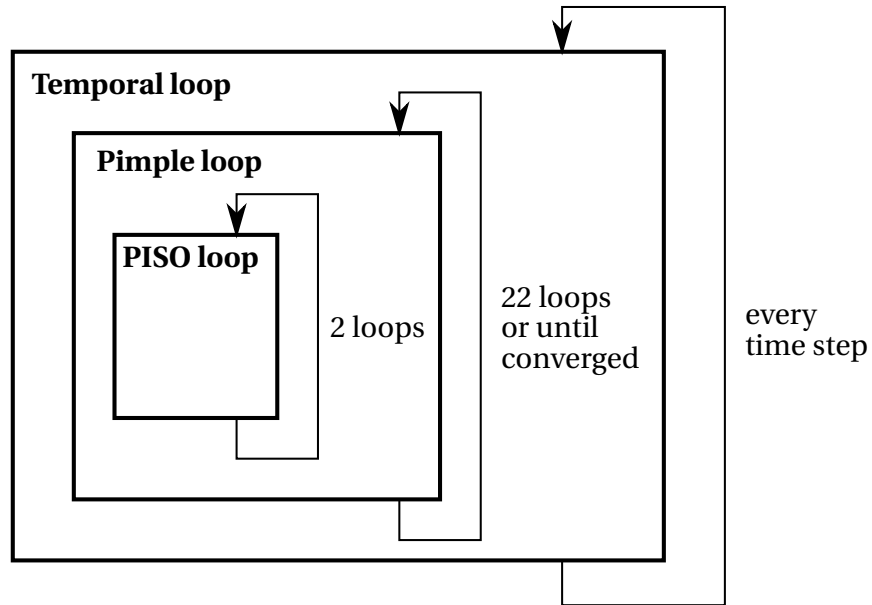


Figure 4.4: Depiction of the three nested loops in the PIMPLE algorithm.

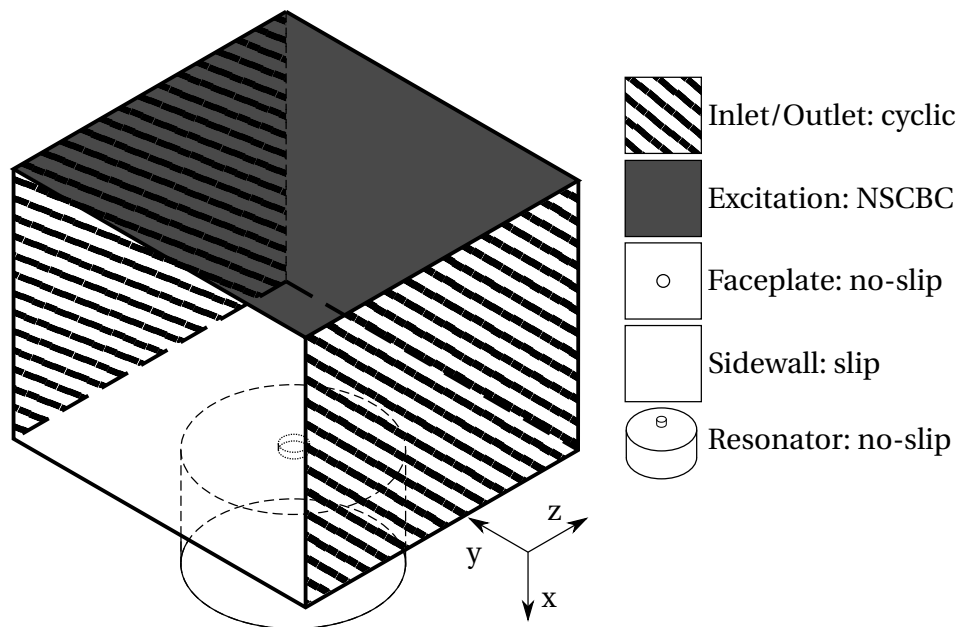


Figure 4.5: Boundary conditions used in the simulation.

4.3 Numerical Setup

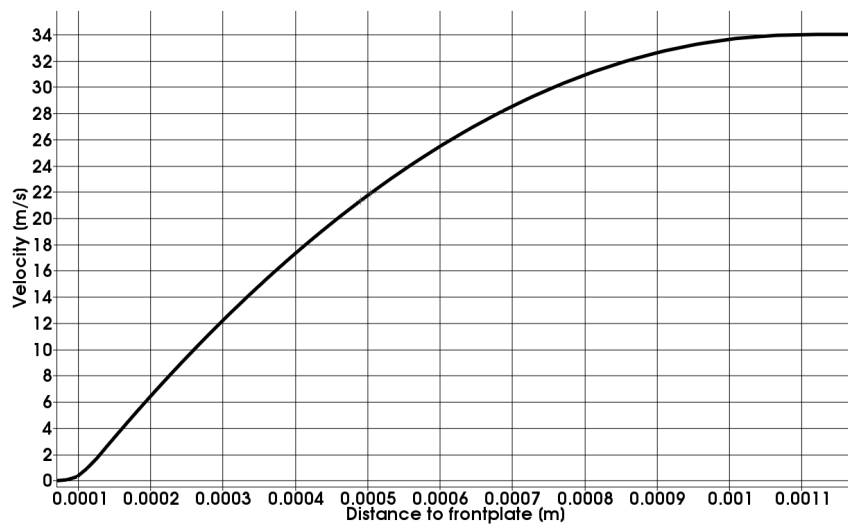


Figure 4.6: Velocity profile of the boundary layer (example at $M = 0.1$).

5 Results of the Numerical Simulations

In this section the simulations will be presented and compared to the analytical and experimental results. Before starting with the actual case studies, the physics involved with a Helmholtz resonator subjected to grazing flow will be explained and visualized. Following up, in Sec. 5.2 and 5.3 the simulation cases will be presented with and without grazing flow.

5.1 The Physics of Helmholtz Resonators with Grazing Flow

In this section, the impact grazing flow has on the resonator behavior will be discussed. Figures 5.1 and 5.2 are used to visualize the in- and outflow behavior of a resonator. Both figures show a cut of a resonator at the neck, with the cavity on the left and the channel on the right side of the picture. The colors on the background indicate the pressure level, ranging from dark blue for lower pressures to dark red for higher pressures. The thick white lines are velocity stream traces, while the black arrows indicate the direction of the velocity vectors. The picture sequence is from left to right, starting with the inflow into the cavity and showing one full cycle.

In the case without grazing flow, seen in Fig. 5.1, the most significant detail about the flow is its symmetry regarding the horizontal and vertical axis. At the beginning of the cycle, fluid starts to flow into the cavity. Because of the relatively low SPL, the flow stays attached to the neck edges. After some time, the pressure inside the cavity is equalizing with the outside pressure, causing a reduction of inflow velocity. When the pressure inside the cavity reaches a certain level, the flow detaches from the wall at the throat edges and small recirculation zones form. As the flow velocity decreases further, those zones increase in size until the turning point, when the flow-direction reverses. As the flow velocity increases again, the circulation zones decrease in size, until the flow reattaches at the throat wall. The outflow cycle shows the same behavior as the previously explained inflow cycle.

With grazing flow, the behavior of the resonator changes dramatically, as seen in Fig. 5.2. The constant overflow generates a circulation inside the neck, breaking the symmetry observable in Fig. 5.1. This circulation zone decreases the effective neck area and restricts the in- and outflow of fluid to the upper and to the lower side. This effect basically decreases the fluctuating mass inside the neck, which, taking Eq. (3.6) into account, leads to an increase of the eigenfrequency. The circulation in the neck causes a second circulation to form inside the cavity itself. Another important observation is the absence of clear cycle phases, that were encountered in the previous case. Disregarding of the pressure difference between cavity and channel, there is always an in- and outflow region, caused by the grazing flow. The in- and outflow velocities change though, which is shown in Fig. 5.3. The velocities are usually higher

5.1 The Physics of Helmholtz Resonators with Grazing Flow

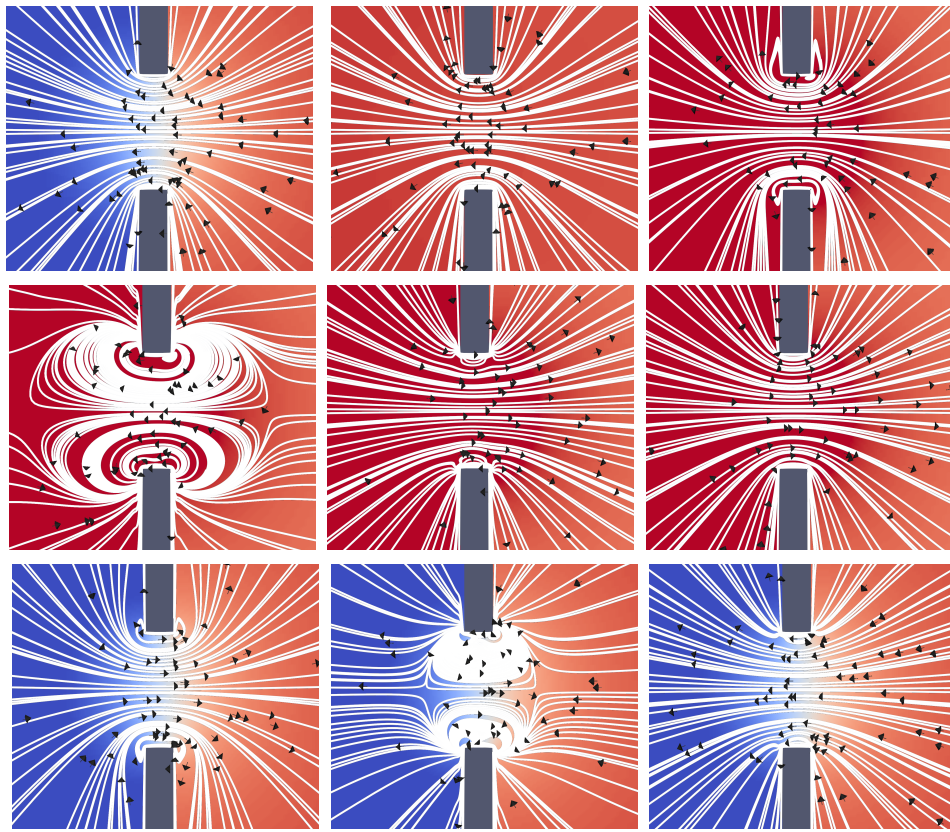


Figure 5.1: Helmholtz resonator cycle at $M = 0$ and $SPL = 75$ dB (cavity on the left). The white lines depict velocity stream traces, with the black arrows indicating flow direction. The colors in the background indicate the pressure level, ranging from blue (low pressure) to red (high pressure).

than without grazing flow, due to the decreased cross section of the throat. Also barely visible, is a slight change in size of the throat circulation zone during the cycle.

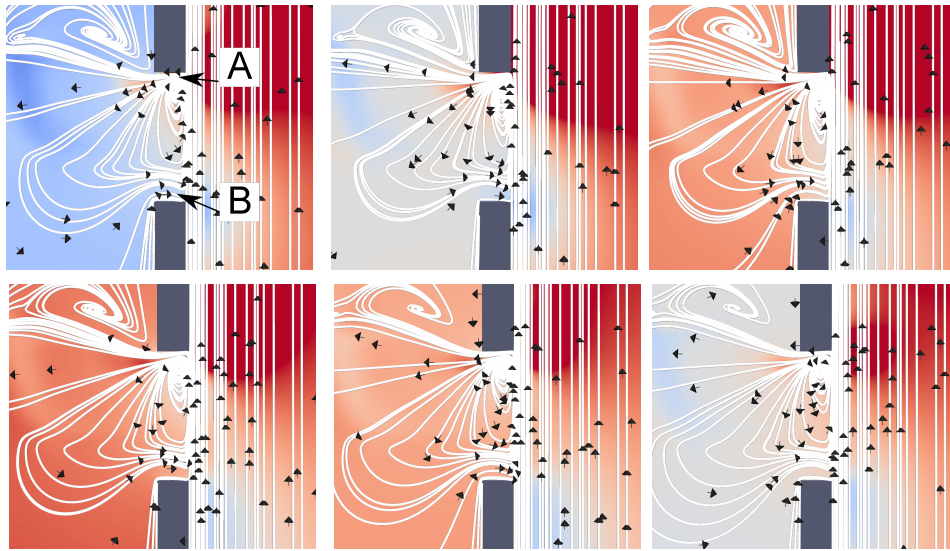


Figure 5.2: Helmholtz resonator cycle at $M = 0.1$ and $SPL = 75$ dB (cavity on the left). The white lines depict velocity steam traces, with the black arrows indicating flow direction. The colors in the background indicate the pressure level, ranging from blue(low pressure) to red(high pressure).

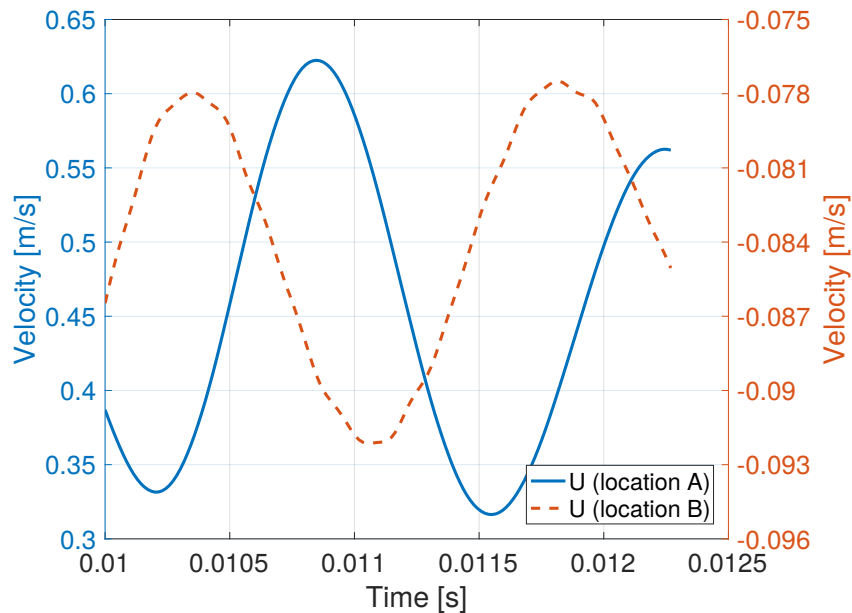


Figure 5.3: In and outflow velocities at the throat walls (locations A and B marked in Fig. 5.2).

5.2 Hersh Helmholtz Resonator Cases

In the work conducted by Hersh et al. [10] different resonators, varying in faceplate thickness, hole diameter and porosity, were investigated. The experiments were done at linear (75 dB) and non-linear regime (120-140 dB), without grazing flow. The resonators consisted of a single circular orifice, which allowed the generation of a fitting resonator mesh using the previously mentioned script, without the need to simplify the resonator geometry.

In the following chapter the original geometry of the Hersh experiment will be denoted as the Hersh75dB geometry, while the geometries used in the numerical simulations will be referred to as Hersh1 and Hersh2, respectively. Geometrical details of the Hersh1 and Hersh2 geometries are listed in Table 5.1 and pictured in Fig. 5.4.

The Hersh2 geometry has the same porosity as the Hersh75dB experiment, but differs from Hersh1 due to its larger faceplate size. The increased faceplate area allows the placement of microphones further away from the resonator opening for a more precise implementation of the in situ impedance eduction method (see Sec. 5.4). The different porosity values cause a slope change of the impedance curve and an increased resistance. To enable a comparison of the simulation results, the definition of an equivalent impedance $z_{\text{sim,eq}}$, mentioned in Förner et al. [7], is used. The equivalent impedance is defined as:

$$z_{\text{sim,eq}} = \frac{A_{\text{fp,sim}}}{A_{\text{fp,exp}}} z_{\text{exp}} , \quad (5.1)$$

or using the porosity defined in Eq. (4.1) with $n = 1$

$$z_{\text{sim,eq}} = \frac{\sigma_{\text{exp}}}{\sigma_{\text{sim}}} z_{\text{exp}} , \quad (5.2)$$

where $A_{\text{fp,sim}}$ and $A_{\text{fp,exp}}$ denote the faceplate area of the simulation and the experiment. The Hersh1 mesh is used for the simulations with grazing flow, while the Hersh2 mesh, which has the same porosity as the original geometry, is used for the simulations without grazing flow to compare it with the experimental data.

	resonator geometry				
	l_0 [mm]	r_0 [mm]	l_{cav} [mm]	r_{cav} [mm]	σ [%]
Hersh75dB	1.59	3.175	25.4	25.4	1.56
Hersh1	1.59	3.175	25.4	25.4	0.46
Hersh2	1.59	3.175	25.4	25.4	1.56
	channel geometry				
	h_{ch} [mm]	l_{ch} [mm]	l_s [mm]		
Hersh1	60	80	86		
Hersh2	60	42.71	47.46		

Table 5.1: Geometric dimensions of the Hersh resonator geometry and the two cases considered.

Case	Frequencies [Hz]								
	500	520	540	550	560	580	600	620	640
Hersh75dB	X	X	X	X	X	X	X	X	X
Hersh1	X	X	X	X	X	X	X		
Hersh2	X	X	X	X	X	X	X	X	X

Table 5.2: Overview of the simulations performed at $M = 0$ and $\text{SPL} = 75$ dB.

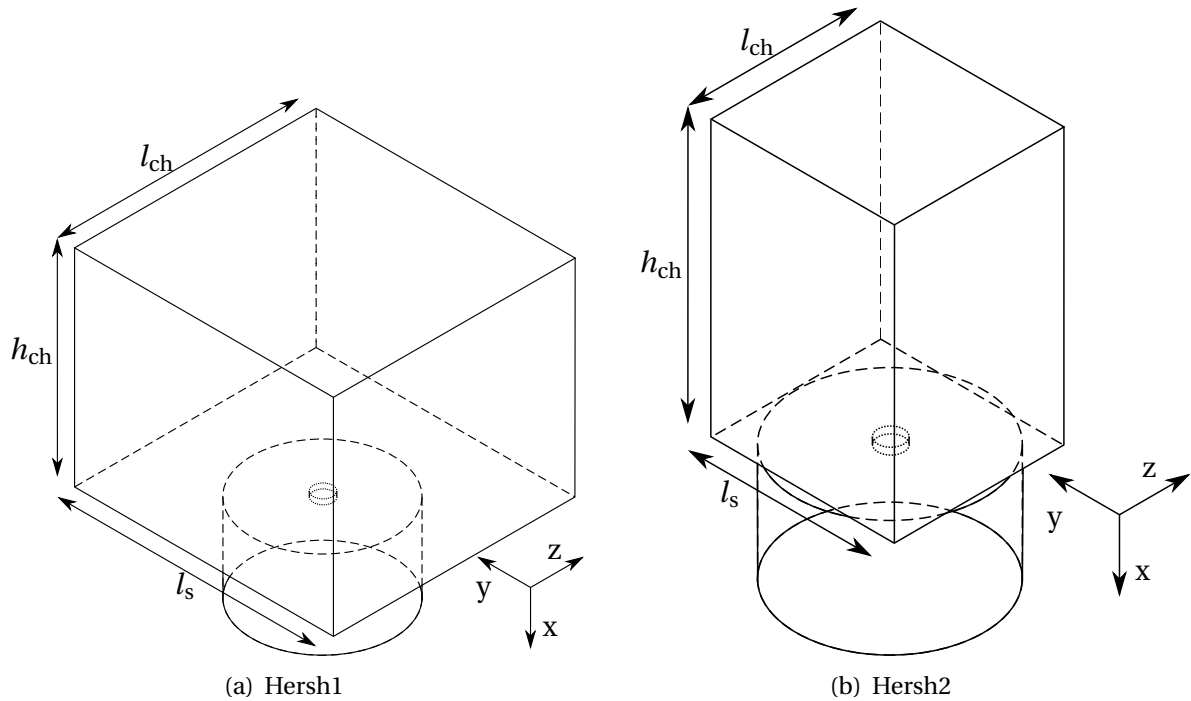


Figure 5.4: Sketch of the Hersh1 and Hersh2 geometries used for the simulations.

5.2.1 Comparison of the Experimental and the Simulation Results

The simulations discussed in this section were performed without grazing flow (Mach Number $M = 0$) and compared to the experimental results. For the simulation, the SPL of the incoming acoustic wave was set to 75 dB, corresponding to the linear regime in this case.

Table 5.2 lists the experiments and simulations that were performed at $M = 0$. Figure 5.5 shows the impedance and reflection coefficient of the Hersh75dB experiment and the Hersh2 case. The resistance of the experiment stays almost constant, slightly above 0.15 with a very flat rise to 0.16 at 640 Hz. The resistance of the Hersh2 case starts at around 0.13, where it also shows the biggest discrepancy with the experimental data. After that it rises to 0.155 at around 540 Hz where it remains approximately constant.

The reactance curves of the experiment and the simulation run parallel, with the simulation data being shifted about 20 Hz to lower frequencies. The effect of this can be seen in the gain of the reflection coefficient, where the simulation has its minimum at 540 Hz, while the experiment has the lowest gain and therefore its eigenfrequency f_{eig} at 560 Hz. Using Eq. (3.9) in combination with Eq. (3.10) the eigenfrequency can be estimated as about 507 Hz which is roughly 10 % lower than the experimental and simulated results. Switching to Eq. (3.11) to calculate $l_{s,\text{corr}}$ at $M = 0$ results in 545 Hz as the eigenfrequency, which is only 1-3 % off the previous results. The impedance was deduced from the CFD simulations, using the impedance tube method. The results of the in situ method will be discussed in Sec. 5.4 .

The method of calculating an equivalent impedance, presented in Sec. 5.2 is only accurate in the linear sound pressure level regime. To show its level of accuracy, a simulation on the Hersh1 mesh without grazing flow was performed and compared to the Hersh2 mesh, where the Hersh1 impedance has been corrected using Eq. (5.2).

The results can be seen in Fig. 5.6. Both the Hersh1 and Hersh2 curves have their resistance maxima at about 550 Hz and then fall off to both sides. After applying the correction there is still a difference between both curves, amounting to about 30% at 500 Hz, 44% at 550 Hz and 33% at 600 Hz. The scaling works quite well regarding the reactance, where the Hersh1 case is only shifted about 10 Hz to lower frequencies.

Figure. 5.7 shows the effect of the correction factor on the impedance. The resistance is scaled to lower values and the slope of the reactance curve is reduced.

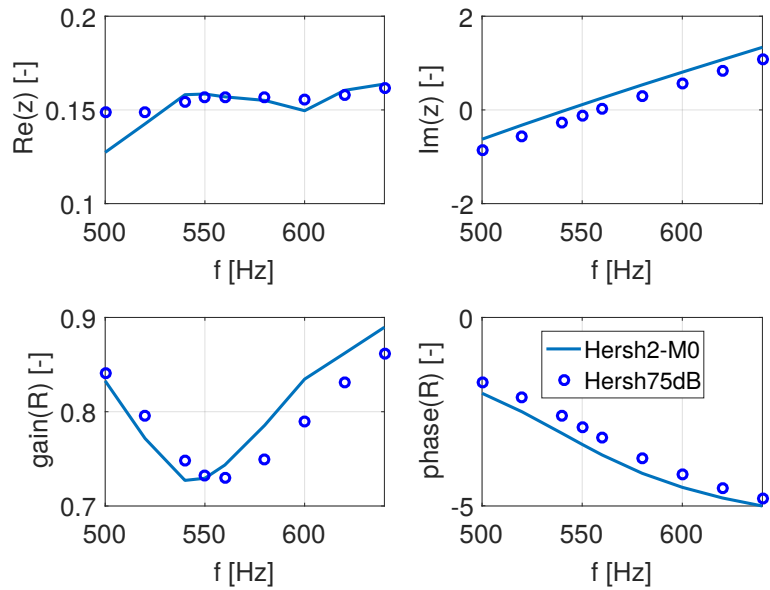


Figure 5.5: Impedance and reflection coefficient at $M = 0$ and $\text{SPL} = 75$ dB.

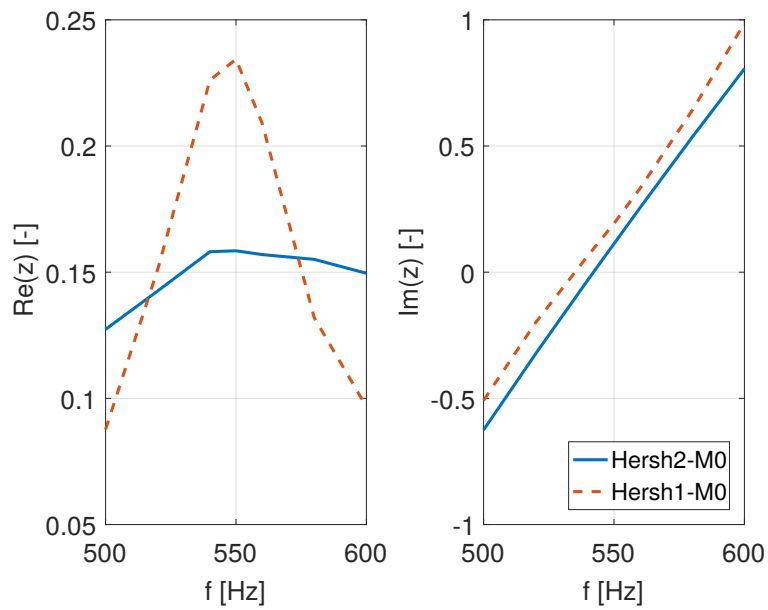


Figure 5.6: Comparison of the Hersh1 and Hersh2 meshes at $M = 0$, using the equivalent impedance method.

5.2 Hersh Helmholtz Resonator Cases

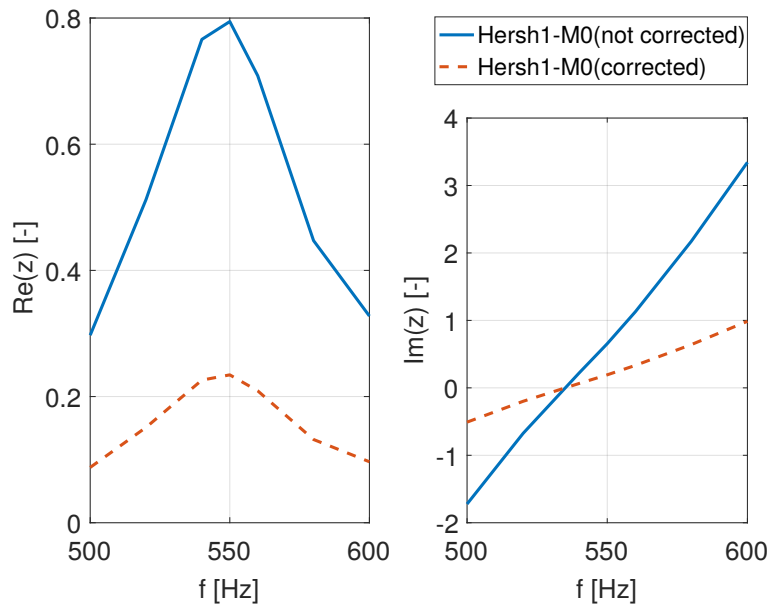


Figure 5.7: Comparison of the Hersh1 case with and without the correction factor defined in Eq. (5.2) .

5.2.2 Analysis of the Simulation Results with Grazing Flow

The simulation with grazing flow was performed using the Hersh1 mesh. For this case, no experimental data was available, but the results were compared to the calculated eigenfrequency, using Eq. (3.6) and (3.11). Table 5.3 lists the frequencies at which the simulations with grazing flow were performed. Here, Hersh1-M0.1 and Hersh1-M0.15 label the simulations on Hersh1 at a grazing flow of $M = 0.1$ and $M = 0.15$, respectively. The frequencies for the Hersh1-M0 case are listed in Table 5.2.

Figure 5.8 shows a massive resistance increase, with increased grazing flow velocity. As explained in Chpt. 3, the energy dissipation (and therefore resistance) is caused by wall friction and flow separation. Both increase in the presence of grazing flow, as explained in Sec. 5.1. The eigenfrequency is also shifted to higher frequencies, as the flow velocity is increased, while the total gain decreases, with the gain-curve being stretched to both higher and lower frequencies. While the phase of the f and g wave were shifted almost 2π at $M = 0$, there is barely any shift visible when grazing flow is present.

Utilizing Eq. (3.6) and (3.11), the eigenfrequency shift due to grazing flow was calculated, the results of these calculations are listed in Table 5.4, with $f_{\text{eig,sim}}$ and $f_{\text{eig,calc}}$ being the eigenfrequency of the simulation as well as the calculation. Δf is the difference in percent between calculated and simulated value.

5.2 Hersh Helmholtz Resonator Cases

Case	Frequencies [Hz]								
	500	550	600	650	675	700	750	800	900
Hersh1-M0.1	X	X	X	X	X	X	X	X	X
Hersh1-M0.15	X		X	X		X	X	X	X

Table 5.3: Simulations performed at $M = 0.1$, $M = 0.15$ and $SPL = 75$ dB.

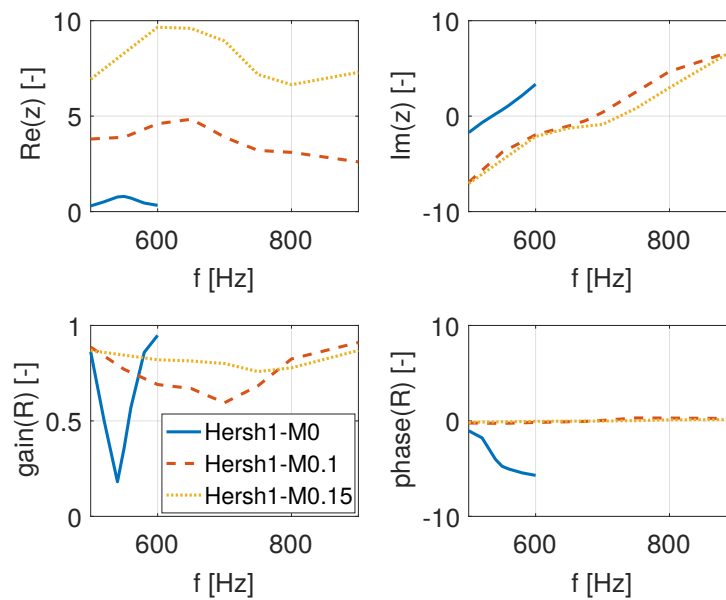


Figure 5.8: Simulation of the Hersh1 geometry with grazing flow.

Mach number	$f_{\text{eig,sim}}$ [Hz]	$f_{\text{eig,calc}}$ [Hz]	Δf [%]
$M = 0$	540	545	+1
$M = 0.1$	700	818	+16.9
$M = 0.15$	750	914	+21.9

Table 5.4: Calculations of eigenfrequency shift.

5.2.3 Numerical Simulation Results of the Whistling Phenomenon

Figure 5.10 shows the simulation results of the Hersh1 geometry at a grazing flow velocity of $M = 0.05$. A negative resistance level implies that the pressure wave that is reflected by the resonator contains more energy than the incoming wave. This is possible, because convective energy from the grazing flow is transferred into acoustic energy, an effect that can be predicted by using the theory about the whistling phenomenon that was presented in Sec. 3.4.

In order to confirm that the observed effect is indeed whistling and not a different effect or even a numerical error, a simulation was conducted without any acoustic excitation and only the grazing flow field. The results of this simulation are shown in Fig. 5.9, which depicts the area average pressure at a reference plane, located 50 mm in front of the resonator. Even without any external acoustic forcing a pressure fluctuation can be observed. A Discrete Fourier Transformation (DFT) reveals that the fluctuation is taking place at about 550 Hz and 83 dB. The frequency corresponds to the eigenfrequency of the system determined in Sec. 5.2.1. Using Eq. (3.17) leads to a critical Strouhal number of $ST_{\text{crit}} = 0.2$. While this number is slightly below the minimum value of 0.38 given for ST_{crit} in Sec. 3.4, it is still close enough to be plausible, especially when considered that the minimum value is highly dependent on the throat diameter.

Section 3.4 described the process of a vortex shedding of the resonator throat edge and then traveling across the resonator opening. This has been visualized in Fig. 5.11. Here, the Q-criterion has been used to visualize the vorticity of the flow field. The high vorticity caused by fluid flowing in and out at the throat edges, makes it challenging to visualize the vortex forming at the lower right corner of the resonator opening, but a structure can be seen forming and expanding towards the opposite throat wall and collapsing periodically.

At higher Mach numbers this effect disappears again, making an impedance analysis possible. This test showed that the whistling effect should be taken into account when analyzing resonators in or near the critical Strouhal number range, especially at low SPLs, as the resulting induced pressure fluctuation will strongly interfere with the intended acoustic pressure signal.

5.2 Hersh Helmholtz Resonator Cases

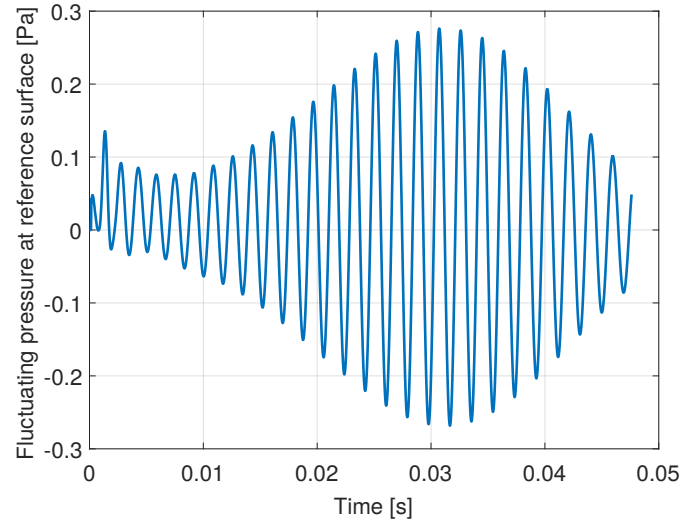


Figure 5.9: Fluctuating pressure p' at reference plane, simulation without acoustic excitation and $M = 0.05$.

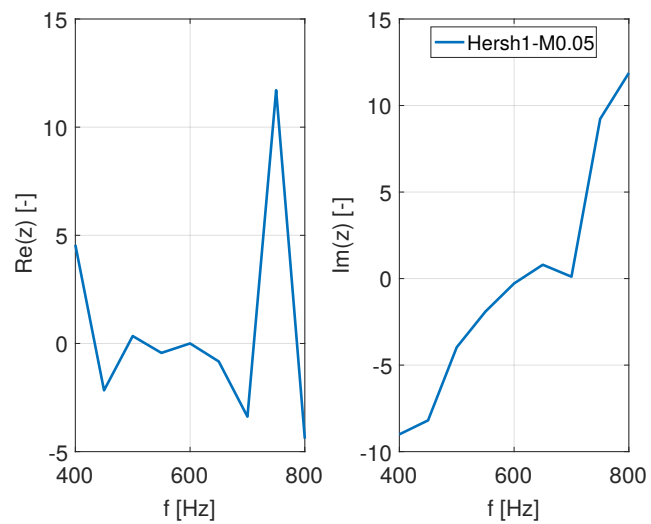


Figure 5.10: Simulation results of the Hersh1-geometry at $M = 0.05$ and $\text{SPL} = 75\text{dB}$.

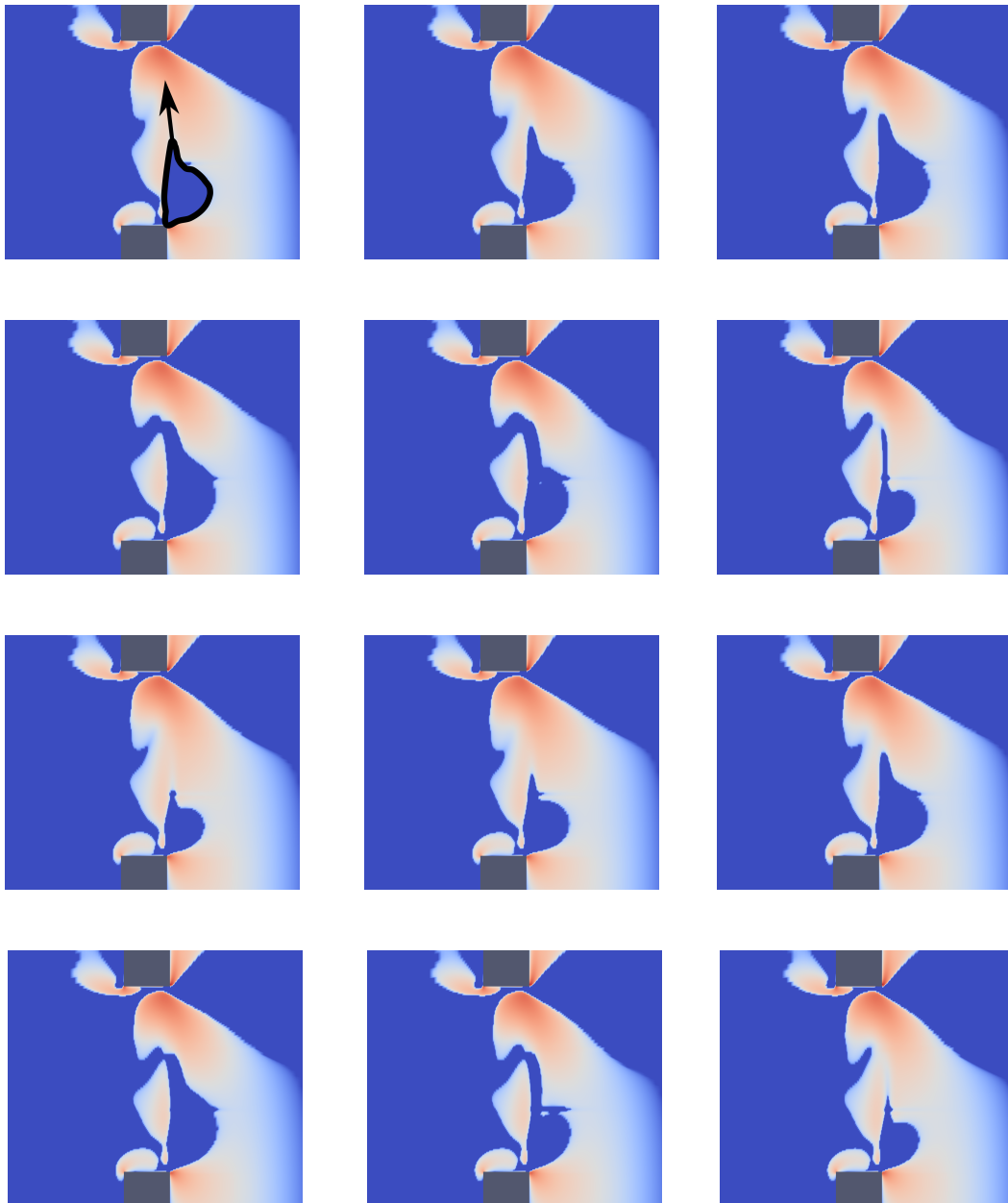


Figure 5.11: Detachment of a vortex at the resonator throat edge, showing two consecutive cycles. The colours represent the Q-Criterion, used to visualize the vorticity.

5.3 Jones Helmholtz Resonator Case

For this section, the geometry and flow parameters are changed in order to duplicate the experimental data presented by Jones et al. [12]. These experiments were conducted using two different experimental setups, both utilizing the impedance tube method, presented in Sec. 3.3.1. The first setup uses only one microphone, which is placed on a traversing bar (TB-experiment), while the second setup has a more classical impedance tube approach, with a total of 95 microphones (95M-experiment) placed in the channel section. In Jones et al. [12] three different liner configurations are presented, out of which the so-called “conventional acoustic liner 1” was chosen for the simulations in this work. The experimental data is labeled “Jones95M” or “JonesTB”, according to the experimental setup. The naming convention for the simulated data follows the “Jones-M0.3-SPL130” scheme, where in this example the Mach number is set as $M = 0.3$ and the sound pressure level equals 130 dB.

The original geometry used hexagonal cavities with an average number of 6.5 holes per cavity, as sketched in Fig. 5.3. To reduce the computational effort and the mesh complexity only resonators with cylindrical cavities and one hole per cavity are meshed and simulated. Thus changes to the original geometry had to be made. First, the hexagonal cavity with an inner diameter d_2 of 9.5mm was converted into a circular cavity with the same cross section. While the outer shape of the resonator may influence its structural rigidity in a real world use case, the fact if its circular or hexagonal shaped should not have any influence on its performance characteristics. From Eq. (3.9) the expression $\omega_{\text{eig}} \sim \sqrt{A_{\text{th}}/V_{\text{cav}}}$ can be deduced. This means that when the number of holes per cavity, and therefore A_{th} , is reduced by the same factor as the cavity volume $V_{\text{cav}} = A_{\text{cav}}l_{\text{cav}}$, then the frequency response of the simplified geometry should stay the same.

A Different scaling method would be to combine the small holes into one big hole. The problem with this method, is that the total neck wall area does not stay constant and therefore the resistance changes. Then, the correction factor $l_{\text{s,corr}}$ (see Eq. (3.10) for further details) will also change, which leads to an eigenfrequency shift.

Table 5.5 lists the geometry for the experiments and the simulations (all simulated cases are combined in the Jones-simulation case).

		resonator geometry					
		l_0 [mm]	r_0 [mm]	l_{cav} [mm]	r_{cav} [mm]	σ [%]	d_2 [mm]
Jones95M/JonesTB		0.64	0.495	38.1	-	6.4	9.5
Jones-simulation		0.64	0.495	38.1	1.9567	6.4	-
		channel geometry					
		h_{ch} [mm]	l_{ch} [mm]	l_s [mm]			
Jones-simulation		30	3.2901	3.6556			

Table 5.5: Jones resonator geometry.

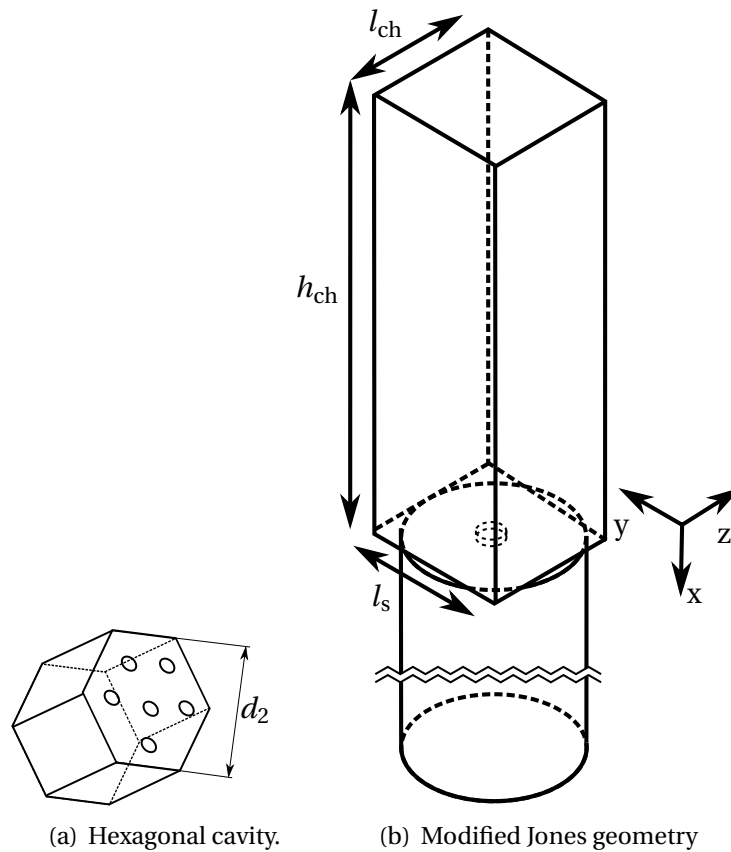


Figure 5.12: Hexagonal cavity geometry and modified Jones geometry for the simulations.

5.3.1 Jones Experimental and Simulation Results with Grazing Flow

In this section, the simulation and experimental results of the Jones geometry will be compared. Table 5.6 lists all parameters that were investigated for the simulation. The experiments by Jones et al. [12], were performed at a SPL of 130 dB, which was measured at a reference microphone located at the front of the impedance tube. Because the exact SPL in front of the resonator neck needed for the simulations was unknown, the first calculations were conducted at $M = 0$ and three different SPLs (130 dB, 135 dB, 140 dB), in order to gain data about the sensitivity of the result to changes of the sound pressure level. The results of those calculations are presented in Fig. 5.13.

As already explained in Chap. 3, it is expected that an increase in SPL leads to higher flow velocities inside the throat, which in turn should lead to a rising non-linear resistance. This can be seen clearly in Fig. 5.13, where the experimental results are located between the simulations at 130 dB and 140 dB. The reactance is only marginally influenced by an increase in SPL, being only shifted to higher frequencies of about 1%. Ideally, if the exact sound pressure level needed for the simulation cannot be determined, the simulations with grazing flow should be performed at a SPL range of about 130 to 140 dB.

Because computations at high SPLs are quite demanding, the simulation for this case was only conducted at an SPL of 130 dB. The results of which can be seen in Fig. 5.14. The resistance determined in the simulation is about 25% to 50% higher than the experimental results. This error could be a result of the geometry differences between experiment and simulation, through to scaling. Another reason certainly is the sound pressure level that was chosen for this simulation and while being close, may not be the same as in the experiments. As already expected from the results in Sec. 5.1 and Sec. 5.2.2 the reactance is shifted to higher frequencies for higher Mach numbers, with the eigenfrequency being shifted from 1500 Hz at $M = 0$ to about 2000 Hz at $M = 0.3-0.4$.

SPL [dB]	Mach number [-]		
	M = 0	M = 0.3	M = 0.4
130	X	X	X
135	X		
140	X		

Table 5.6: Simulations performed at at 1000/1500/2000/2500 and 3000 Hz.

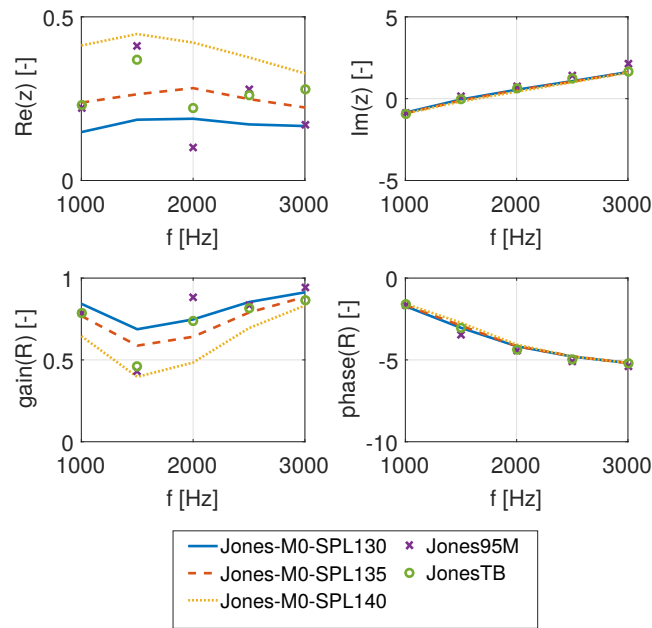


Figure 5.13: Simulation of the Jones geometry at $M = 0$ and varying SPLs.

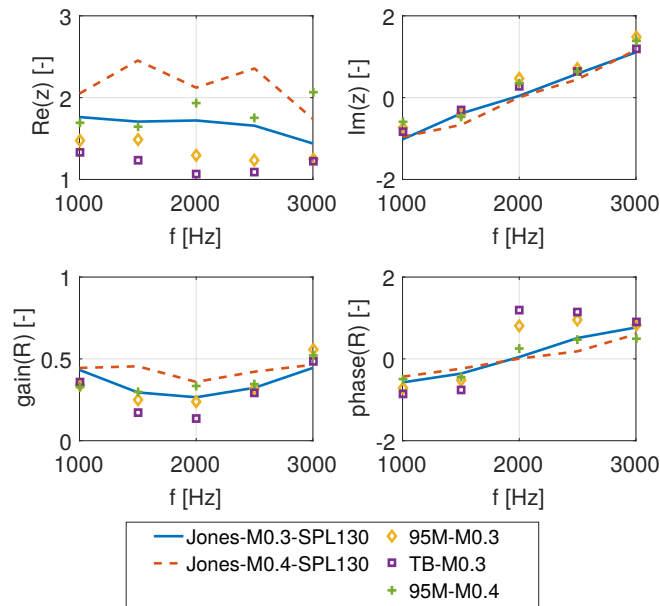


Figure 5.14: Simulation of the Jones geometry at $M = 0.3$, $M = 0.4$ and $SPL = 130$.

5.4 Evaluation of the In Situ Method

In the previous chapters, the impedance was determined using the impedance tube method, presented in Sec. 3.3.1. In this section, the previous simulation results will be compared to the results obtained using the in situ method, which is explained in detail in Sec. 3.3.2. The main goal is to evaluate the compliance of both methods, especially at higher grazing flow velocities. The in situ method has been used in numerous other publications, because it is easy to implement and well established in normal incidence scenarios, as for example mentioned by Zhang [20].

In order to separate the turbulent and acoustic pressure fluctuations from the pressure sensor data, several pressure probes were placed on the faceplate and backplate of the Jones and Hersh mesh and their results later averaged in post-processing. As the SPL and maximum grazing flow speed in the Hersh1-case (see Sec. 5.2) were lower, namely $M = 0.15$ and $SPL = 75$ dB, less probes are needed, because the turbulent fluctuations are less strong. In the Jones-case (see Sec. 5.3) however, the SPL is in the non-linear regime with $SPL = 130$ dB and the maximum grazing flow velocity is more than doubled compared to the Hersh1-case, so more turbulent fluctuations are expected and therefore more probes are needed on the frontplate. The probe number and placement at the backplate is less important.

For the Hersh1-case, 24 probes were placed on the frontplate with a minimum distance from the center of $3d_0$, while for the Jones-case the number of probes was raised to 50 with a minimum distance to the center of about $1d_0$ due to space constraints. The Hersh and Jones cases had 9 and 20 probes at the backplate, respectively.

Figures 5.15 and 5.16 show the results of the impedance tube method and the in situ method for varying frequencies and grazing flow velocities. While at $M = 0$ both methods match almost exactly, the discrepancies increase in both cases for higher Mach numbers, with the in situ method underestimating the resistance in respect to the impedance tube method. The reactance is shifted to lower frequencies when using the in situ method. The results show that while using the in situ method in resonators without grazing flow may lead to accurate results, the impedance tube method should be preferred if grazing flow is present. While it is easy to implement the impedance tube method in a numerical simulation, it may not always be possible in experiments.

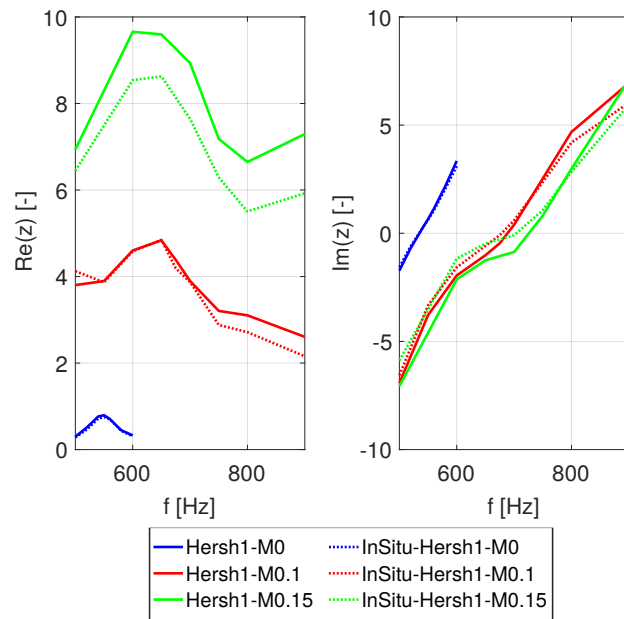


Figure 5.15: Comparison of the impedance tube and the in situ method using the Hersh1 geometry at SPL = 75 dB and $M = 0 \mid 0.1 \mid 0.15$.

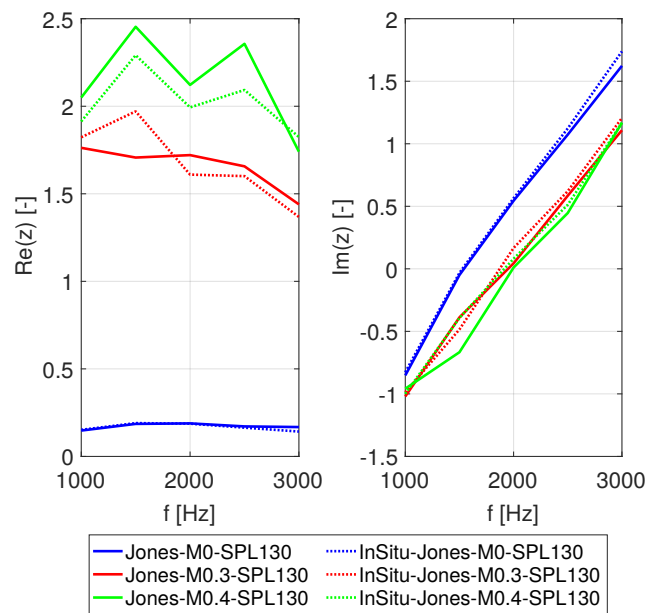


Figure 5.16: Comparison of the impedance tube and the in situ method using the Jones geometry at SPL = 130 dB and $M = 0 \mid 0.3 \mid 0.4$.

6 Summary and Conclusion

This work investigates the possibilities of using CFD calculations in OpenFOAM to accurately portray the behavior of Helmholtz resonators when subjected to grazing flow. Here, one major difficulty is the scaling of multi-throat resonators to a single-throat single-cavity geometry, without influencing its impedance. Additionally, the accuracy of two different impedance determination methods, namely the impedance tube method and the in situ method, was analyzed, in particular their sensitivity to the grazing flow velocity. The results were validated using experimental results by Hersh et al. [10] as well as Jones et al. [12] and also compared to eigenfrequency estimations, using analytical formulas.

In the first step, the goal was to gain basic understanding of a Helmholtz resonator and its behavior when subjected to grazing flow. For this purpose the Hersh-geometry [10] was chosen, since it was already a single-port geometry and required no scaling. The results of the Hersh-geometry simulation without grazing flow matched very well with the experiments, with almost identical resistance values and a minor 10 Hz shift in the reactance curve. Then, simulations with a grazing flow velocity of $M = 0.1$ and $M = 0.15$ were conducted and compared with analytical estimations as there was no experimental data available for these cases. In comparison, the analytical results overestimated the simulation by 1% to 20% with the difference increasing at higher flow velocities. Overall, it was shown that the eigenfrequency increases as expected and that the damping efficiency of the resonator decreases at higher velocities for small SPLs. The reason for that being the inability of the low energy acoustic wave to influence the high energy grazing flow field.

After the validity of the overall simulation method was shown, the accuracy of the numerical simulation with grazing flow had to be confirmed. Therefore the Jones-geometry [12] was used, as there was experimental data with grazing flow available for this case, that used a multi-port configuration of about 6.5 resonator openings per cavity. In order to scale the multi-port geometry without changing its impedance, the number of openings per cavity was reduced to one, while also reducing the overall volume of the resonator. As the exact SPL for the single port geometry was unknown, the first simulations were conducted at various sound pressure levels and in absence of grazing flow. The first results confirmed the validity of the scaling method, as the eigenfrequency and overall reactance of simulation and experiment match well. As expected, the resistance was very sensible to SPL changes, with an maximum relative error of about 25% compared to the experiment. The results involving grazing flow showed a similar behavior, as the reactance of simulation and experiment matched very well with only minor deviations, while the resistance was overestimated by the experiment by about 25 to 50%.

Furthermore, the difference of the impedance eduction methods at rising grazing flow

velocities was determined. While the two methods provided the same results without grazing flow, the difference increased at higher velocities. This result underlines the difficulties of impedance determination once grazing flow is involved.

An interesting effect was encountered when simulating the Hersh-geometry with a grazing flow velocity of $M = 0.05$. Here, the resonator did not dampen the incoming pressure fluctuation, but seemingly increased its amplitude instead. This effect can be explained with the theory of the whistling phenomenon, which is described in Tonon et al. [18], stating that for a certain combination of flow velocity and throat diameter acoustic fluctuations can be induced by interactions with the grazing flow.

The last paragraphs will present a couple of changes that could be implemented to improve the simulation results, or to gain further insight into the working principles of Helmholtz resonators. In order to get more accurate results with the Jones-geometry [12], it would be helpful to find a method to better determine the exact sound pressure level needed for the pressure excitation in the simulation. At the moment the simulations are being conducted at a SPL of 130 dB, but as the resistance is quite sensitive to SPL changes, a more accurate SPL value would be desirable.

The boundary layer of the grazing flow was modeled using a 1 mm thick boundary layer with a simple quadratic profile. In order to improve this model, boundary layer theory or other simulations could be used to create a more accurate profile, either laminar or turbulent. Then several studies should be conducted to determine the effect of the boundary layer type (laminar/turbulent) and the thickness, on the impedance of the resonator. Another interesting case study would be the investigation of the effects of chamfered edge geometry on the performance of the resonator, as has been already done by Förner et al. [8] for resonators without grazing flow.

Appendices

A Implementation of the In Situ Method in Matlab

The following function is a Matlab implementation of the in situ method presented in Sec. 3.3.2

Listing A.1: Matlab implementation of the in situ method.

```
function [ z_dean ] = dean( freq, path, Case )
%Implements the in situ method (here also called Dean's Method).
%Input is the frequency [Hz] and the path to the simulation Case.
%Output is the normalized impedance z_dean.
5
a_inf = 343;           %speed of sound [m/s]
k = (freq*2*pi)/a_inf; %wave number [rad/m]
cutoff_time = 2/freq; %cutoff-time after n cycles [s]
10
%loadAllTimesProbes loads all probe data for one Case
data_probes = loadAllTimesProbes(Case,'path',path);
%cut4fft_probes cuts off the pressure data at the cutoff time
data_probes = cut4fft_probes(data_probes,freq,cutoff_time);
15
%names contains an array of strings,consisting of the positions of the
%probes
names = data_probes.ExperimentName;
%get sampling instants
times = data_probes.SamplingInstants{1,1};
20
%Find the number of probes on the Frontplate (at X=0)
A = sum(strcmp(names,'X_0_Y',5));
%Determine the total number of probes
B = length(names);
25
%If no probes have been found than switch to Jones case
%(Jones-probes are located at X=-1e-06)
if A == 0
    %%Jones case
30
    %Total height of the Jones cavity [m]
    H = 0.03874;
    %Correction factor is only needed for the Hersh1 case.
    corr = 1;
    %Find the number of probes on the Frontplate (at X=-1e-06)
35
    A = sum(strcmp(names,'X_-1e-06_Y',10));
    %get pressure data from the backplate probes
```

```

    %and convert it into matrix
    p_backplate = cell2mat(data_probes(:, [], 'p', A+1:B).u);
    %get pressure data from the frontplate probes
    %and convert it into matrix
40 p_frontplate = cell2mat(data_probes(:, [], 'p', 1:A).u);
else
    %%Hersh1 case
    %Total height of the Hersh case [m]
45 H = 0.02699;
    %correction factor needed, because the Hersh1-geometry frontplate is
    %3.39 times bigger than the cavity area.
    corr = 3.39;
    p_backplate = cell2mat(data_probes(:, [], 'p', 1:(B-A)).u);
50 p_frontplate = cell2mat(data_probes(:, [], 'p', (B-A+1):B).u);
end

%Determine an average pressure array from all the frontplate sensors.
p_frontplate = mean(p_frontplate(:, :), 2);
55 %Determine an average pressure array from all the backplate sensors.
p_backplate = mean(p_backplate(:, :), 2);
%subtract mean value to get the fluctuating pressure
p_frontplate = p_frontplate - mean(p_frontplate);
p_backplate = p_backplate - mean(p_backplate);
60 %place corrected data into new iddata object
data_mean = iddata([], [p_frontplate, p_backplate], [], 'SamplingInstants'...
    , times, 'InputName', {'p-frontplate'; 'p-backplate'});

%perform fourier transformation of the pressure data
65 fft_data = fft(data_mean);
%determine the maximum fourier coefficients
%(max_coef is a complex number/vector)
[max_coef, n] = max(abs(fft_data.u));
%Determine phase shift between frontplate and backplate pressure
70 angle_f = angle(fft_data.u(n(1), 1));
angle_b = angle(fft_data.u(n(2), 2));
phase_shift = angle_f - angle_b;

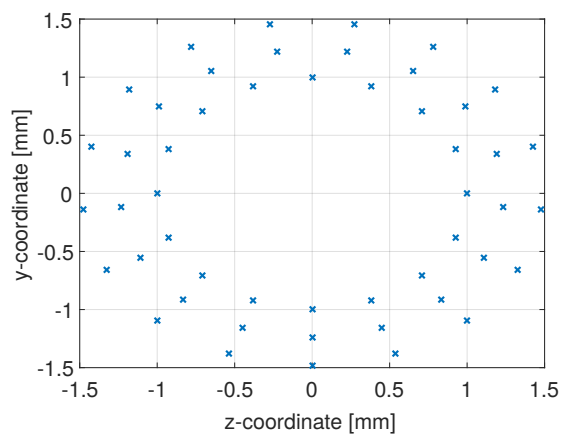
%Calculate the impedance z using the in situ method
75 z_dean = -1i * (max_coef(1)/max_coef(2)) * ...
    (exp(1i*phase_shift))/sin(k*H/corr);
end

```

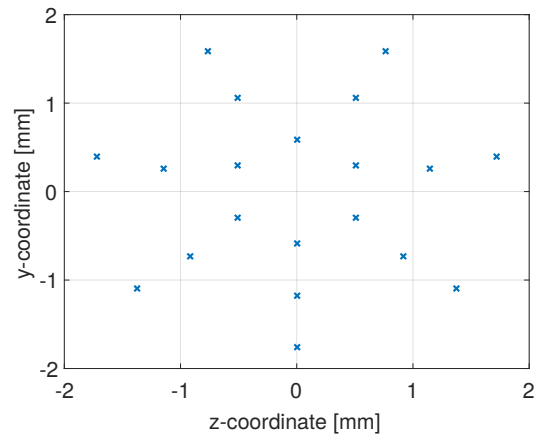
B Calculation of Probe Coordinates in Matlab

This script calculates the coordinates of the pressure probes, needed for the evaluation of the in situ method, as shown in Sec. 5.4 . The coordinates are automatically written in a text file with the correct formatting.

Figure B.1 shows the calculated probe locations, after the script has been executed. Note the circular empty zone in the center of the frontplate , which is necessary to maintain a safety distance from the regions with high turbulent pressure fluctuations.



(a) Frontplate probe positions.



(b) Backplate probe positions.

Figure B.1: Coordinates of the frontplate and backplate probes. Example shows the probes for the Jones geometry.

Listing B.1: Matlab script to calculate the probe positions for the evaluation of the in situ method

```
%Script to calculate the probe positions  
%Output is a textfile in correct formatting, with the coordinates of the  
%probes on the backplate and the frontplate  
  
5 %Minimum distance to front/backplate [m]  
delta_null = 10^-6;  
  
%%Frontplate  
%Minimum distance to the resonator center [m]  
10 rf_min = 0.001;  
%Width of the channel [m]  
H_can_YZ = 0.0032901;  
%Maximum radius for probe positioning  
rf_max = H_can_YZ/2;  
15 %Safety distance from walls  
rf_max = 0.9 * rf_max;  
%Number of rows of frontplate probes  
rowsf = 3;  
%Total number of frontplate probes  
20 n_f = 50;  
  
%Cavity radius [m]  
r_cav = 0.0019567;  
%Depth of the resonator [m]  
25 l_res = 0.0381;  
%Length of the neck [m]  
l_0 = 0.00064;  
%Total length of the resonator  
l_cav = l_res + l_0;  
30 %Safety distance from cavity wall  
r_b_max = 0.9 * r_cav;  
%Number of rows of backplate probes  
rowsb = 3;  
%Total number of backplate probes  
35 n_b = 20;  
  
n_rowf = zeros(rowsf,1);  
n_rowb = zeros(rowsb,1);  
  
40 %Distribute Probes to all frontplate rows  
for i=1:rowsf  
    n_rowf(i) = floor(n_f/rowsf);  
end  
n_remainf = n_f-(rowsf * floor(n_f/rowsf));  
45 jj = rowsf;  
while n_remainf > 0  
    n_rowf(jj) = n_rowf(jj) +1;  
    jj = jj -1;  
    n_remainf = n_remainf -1;
```

```

50 end

%Distribute Probes to all backplate rows
for i=1:rowb
    n_rowb(i) = floor(n_b/rowb);
55 end
n_remainb = n_b-(rowb * floor(n_b/rowb));
jj = rowb;
while n_remainb > 0
    n_rowb(jj) = n_rowb(jj) +1;
60 jj = jj -1;
    n_remainb = n_remainb -1;
end

%Calculate the positional angle of frontplate rows
65 phi_f = zeros(n_rowf(rowf),rowf);
for j=1:rowf
    for i=1:n_rowf(j)
        phi_f(i,j) = (2*pi)/n_rowf(j) * (i-1);
    end
70 end

%Calculate the positional angle of backplate rows
phi_b = zeros(n_rowb(rowb),rowb);
for j=1:rowb
75     for i=1:n_rowb(j)
        phi_b(i,j) = (2*pi)/n_rowb(j) * (i-1);
    end
end

80 %Calculate the distance of every frontplate row to the center of the
%faceplate
r_rows_f = zeros(rowf,1);
for i = 1:rowf
    r_rows_f(i) = rf_min + (i-1) * ((rf_max-rf_min)/(rowf-1));
85 end

%Calculate the distance of every backplate row to the center of the
%backplate
r_rows_b = zeros(rowb,1);
90 for i = 1:rowb
    r_rows_b(i) = i*(r_b_max/rowb);
end

%Get frontplate probe coordinates
95 fprobe_pos = cell(n_rowf(rowf),rowf);
for j=1:rowf
    for i=1:n_rowf(j)
        fprobe_pos{i,j} = {-delta_null,-r_rows_f(j) * ...
            cos(phi_f(i,j)),r_rows_f(j) * sin(phi_f(i,j))};
100 end

```

```

end

%Get backplate probe coordinates
bprobe_pos = cell(n_rowb(rowsb),rowsb);
105 for j=1:rowsb
    for i=1:n_rowb(j)
        bprobe_pos{i,j} = {(l_cav-delta_null),-r_rows_b(j) * ...
            cos(phi_b(i,j)),r_rows_b(j) * sin(phi_b(i,j))};
    end
110 end

%Create textfile in OpenFOAM formatting with the probe coordinates
n = 1;
115 fdebugy = zeros(n_f,1); %for debugging, not needed for script
fdebugz = zeros(n_f,1); %for debugging, not needed for script
fileID = fopen('probes_test.txt','w');
fprintf(fileID,'X \t Y \t Z \t\t Frontplate Probes\n');
for j=1:rowsf
120     for i=1:n_rowf(j)
        pos = cell2mat(fprobe_pos{i,j});
        x = pos(1);
        y = pos(2);
        z = pos(3);
125     fdebugy(n)=y;
        fdebugz(n)=z;
        fprintf(fileID,'%1.6f %1.6f %1.6f) \t // f%d\n',x,y,z,n);
        n = n+1;
    end
130 end

nn = 1;
bdebugy = zeros(n_b,1);
bdebugz = zeros(n_b,1);
135 fprintf(fileID,'X \t Y \t Z \t\t Backplate Probes\n');
for j=1:rowsb
    for i=1:n_rowb(j)
        pos = cell2mat(bprobe_pos{i,j});
        x = pos(1);
140     y = pos(2);
        z = pos(3);
        bdebugy(nn)=y;
        bdebugz(nn)=z;
        fprintf(fileID,'%1.6f %1.6f %1.6f) \t // b%d\n',x,y,z,nn);
145     nn = nn+1;
    end
end
fclose(fileID);

```

Bibliography

- [1] rhoPimpleFoam.C (code-annotations). Available at <https://github.com/OpenFOAM/OpenFOAM-2.2.x>; downloaded on 2017-01-21.
- [2] The PISO algorithm in OpenFOAM. Available at https://openfoamwiki.net/index.php/OpenFOAM_guide/The_PISO_algorithm_in_OpenFOAM; visited on 2017-01-21.
- [3] N.A. Adams. *Fluidmechanik I - Skript*. Lehrstuhl für Aerodynamik und Strömungsmechanik, 2013.
- [4] A. M. Binnie. Self-induced waves in a conduit with corrugated walls ii. experiments with air in corrugated and finned tubes. *Proceedings of the Royal Society of London A: Mathematical, Physical and Engineering Sciences*, 262(1309):179–191, 1961.
- [5] P.D. Dean. An in situ method of wall acoustic impedance measurement in flow ducts. *Journal of Sound and Vibration*, 34(1):97 – 130, 1974.
- [6] K. Ehrenfried. *Strömungsakustik: Skript zur Vorlesung*. Berliner Hochschulskripte. Mensch-und-Buch-Verlag, 2004.
- [7] K. Förner, A. Cárdenas Miranda, and W. Polifke. Mapping the Influence of Acoustic Resonators on Rocket Engine Combustion Stability. *Journal of Propulsion and Power*, 31(4):1159–1166, July 2015.
- [8] K. Förner, M. A. Temiz, W. Polifke, I. Lopez Arteaga, and A. Hirschberg. On the non-linear Influence of the Edge Geometry on Vortex Shedding in Helmholtz Resonators. In *22nd International Congress on Sound and Vibration (ICSV22), Florence, Italy*, 2015.
- [9] G.D. Garrison, A.C. Schnell, C.D. Baldwin, and P.R. Russell. Suppression of Combustion Oscillations with Mechanical Damping Devices. Interim Report PWA FR-3299, Pratt & Whitney Aircraft, 1969.
- [10] A. S. Hersh, B. E. Walker, and J. W. Celano. Helmholtz Resonator Impedance Model, Part 1: Nonlinear Behavior. *AIAA Journal*, 41(5):795–808, May 2003.
- [11] U. Ingard. On the Theory and Design of Acoustic Resonators. *The Journal of the Acoustical Society of America*, 25(6):1037–1061, November 1953.

BIBLIOGRAPHY

- [12] M. Jones, W. Watson, T. Parrott, and C. Smith. Design and Evaluation of Modifications to the NASA Langley Flow Impedance Tube. In *10th AIAA/CEAS Aeroacoustics Conference*, Manchester, Great Britain, May 2004. American Institute of Aeronautics and Astronautics.
- [13] J. J. Keller and E. Zauner. On the use of helmholtz resonators as sound attenuators. *Zeitschrift für angewandte Mathematik und Physik ZAMP*, 46(3):297–327, 1995.
- [14] P.K. Kundu, I.M. Cohen, and D.R. Dowling. *Fluid mechanics*. Elsevier, 2015.
- [15] T. Poinsoot and S. K. Lele. Boundary Conditions for Direct Simulation of Compressible Viscous Flows. *J. Comp. Phys.*, 101(1):104–129, 1992.
- [16] W. Polifke, J. van der Hoek, and B. Verhaar. Everything you always wanted to know about f and g. -Skript, 2016.
- [17] E. J. Rice. A model for the acoustic impedance of a perforated plate liner with multiple frequency excitation. NASA Technical Memorandum, Cleveland, Ohio, 1971.
- [18] D. Tonon, B.J.T. Landry, S.P.C. Belfroid, J.F.H. Willems, G.C.J. Hofmans, and A. Hirschberg. Whistling of a pipe system with multiple side branches: Comparison with corrugated pipes. *Journal of Sound and Vibration*, 329(8):1007–1024, April 2010.
- [19] H. Von Helmholtz. *On the Sensations of Tone as a Physiological Basis for the Theory of Music*. Longmans, Green, 1912.
- [20] Q. Zhang. *Direct numerical investigation and reduced-order modeling of 3-D honeycomb acoustic liners*. PhD thesis, University of Illinois at Urbana-Champaign, 2014.